Time-Dependent Density Functional Theory for X-Ray Absorption Spectra: Comparing the Real-Time Approach to Linear Response

John M. Herbert,[1,2*] Ying Zhu,[1,2] Bushra Alam,[1] and Avik Kumar Ojha[1]
[1] *Department of Chemistry & Biochemistry, The Ohio State University, Columbus, Ohio, 43210 USA and*
[2] *Chemical Physics Graduate Program, The Ohio State University, Columbus, Ohio, 43210 USA*
(Dated: August 26, 2023)

Abstract

We simulate x-ray absorption spectra at elemental K-edges using time-dependent density functional theory (TDDFT), in both its conventional linear-response implementation and also its explicitly time-dependent or "real-time" formulation. Real-time TDDFT simulations enable broadband spectra calculations without the need to invoke frozen occupied orbitals ("core/valence separation"), but we find that these spectra are often contaminated by transitions to the continuum that originate from lower-energy core and semi-core orbitals. This problem becomes acute in triple-ζ basis sets although it is sometimes sidestepped in double-ζ basis sets. Transitions to the continuum acquire surprisingly large dipole oscillator strengths, leading to spectra that are difficult or impossible to interpret. Meaningful spectra can be recovered by means of a filtering technique that decomposes the spectrum into contributions from individual occupied orbitals, and the same procedure can be used to separate L- and K-edge spectra arising from different elements within a given molecule. In contrast, conventional linear-response TDDFT requires core/valence separation but is free of these artifacts. It is also significantly more efficient than the real-time approach, even when hundreds of individual states are needed to reproduce near-edge absorption features and even when Padé approximants are used to reduce the real-time simulations to just 2–4 fs of time propagation. Despite the cost, the real-time approach may be useful to examine the validity of the core/valence separation approximation.

1 Introduction

Quantum chemistry is currently witnessing a surge of interest in x-ray spectroscopy,[1–9] catalyzed by the emergence of new technologies including coherent ultrahigh harmonic generation,[10] which has enabled ultrafast time resolution at x-ray wavelengths.[11–13] This technology, which is now available in tabletop laser systems,[14] has enabled both x-ray photoelectron spectroscopy and also x-ray absorption spectroscopy (XAS) of solution-phase systems,[15–18] as well as surface-sensitive ultrafast spectroscopy at extreme ultraviolet (XUV) wavelengths.[19] Insofar as XAS is a widely-used tool to interrogate bonding and oxidation states, these advances offer the possibility to study element-specific charge dynamics with ultrafast time resolution. Electronic structure theory will undoubtedly play a major role in interpreting the results.[20]

Although there are multiple ways to obtain excited electronic states from density-functional theory (DFT) calculations,[21] the most widely used approach is the linear-response (LR) formulation of time-dependent (TD-)DFT,[21–26] which we call LR-TDDFT in the present work, but which is so ubiquitous in modern quantum chemistry that it is usually just called "TDDFT". Its computational cost and storage requirements scale as $\mathcal{O}(no^2v^2)$ and $\mathcal{O}(nov)$,[21,25] respectively, where o and v are the number of occupied and virtual molecular orbitals (MOs), and n is the number of excited states. These states must be computed using iterative eigensolvers,[27–30] and the number of excited states that is required to reach core-level excitation energies is prohibitively large unless an active-space approximation is invoked.[31] By including only a few core orbitals along with the full virtual space, core-to-valence excitations appear as the lowest-energy states in the spectrum. In many-body theory, this active-space approximation is known as "core/valence separation" (CVS),[1,32–37] whereas in LR-TDDFT it has also been called a "restricted excitation window".[5,38] It amounts to freezing most of the occupied MOs.

For K-edge transitions, meaning those that originate from 1s orbitals in the occupied space, the CVS approximation introduces errors of < 1 eV in absolute excitation energies,[39,40] which amount to element-specific shifts.[39] It is less clear what the errors might be for L- or M-edge excitations, since these originate from orbitals with higher principle quantum number that may not be energetically separated from other valence orbitals. Although interior eigensolvers could be used for core-level excitations,[40–42] that approach has not yet been widely deployed.

What makes LR-TDDFT attractive is that its cost per iteration exhibits the same scaling as ground-state Fock matrix construction,[25,43–45] and that cost is asymptotically quadratic (rather than quartic) with respect to system size.[25,44] That said, the cost does grow with the number of states, and hundreds of excited states may be required to compute near-edge x-ray adsorption fine structure (NEXAFS) spectra. As such, LR-TDDFT cal-

*herbert@chemistry.ohio-state.edu

culations of semiconductors and other systems with large densities of states might be prohibitively expensive,[46–48] even if the corresponding ground-state DFT calculation is feasible.

Some of these limitations can be overcome using an alternative formulation of TDDFT in which broadband spectra are obtained via solution of the time-dependent Kohn-Sham (TDKS) equation,[49–53] in what is sometimes called "real-time" TDDFT.[21,54,55] This is potentially attractive for XAS because the computational resource requirements are independent of the number of excited states. Conceptually, a broadband spectrum is obtained from the Fourier transform of the fluctuating dipole moment of a perturbed ground state, with a spectral resolution that improves with additional propagation time. Unlike LR-TDDFT, the total memory requirement is similar to that of a ground-state DFT calculation and does not scale with n. The cost does increase for higher-energy excited states because a smaller integration time step is required, since higher-lying resonances correspond to higher-frequency Fourier components of the signal. That said, the time-step error might be more easily controlled as compared to errors engendered by truncation of the excitation space in LR-TDDFT, because the former can be reduced systematically using smaller time steps and longer simulation times, at the expense of additional computational time. In contrast, enlarging the LR-TDDFT excitation space may encounter hardware (storage) limitations for large systems and/or large densities of states.

The TDKS and LR-TDDFT approaches are formally equivalent,[21–24,51] in the limit of a weak perturbation to the ground state, provided that the full basis of $o \times v$ excitation vectors is used in the LR-TDDFT approach. (This equivalence has also been demonstrated in practical calculations.[56,57]) TDKS simulations can thus reveal the true TDDFT spectrum in the absence of any truncations, which may be important for characterizing how the CVS approximation impacts L- and M-edge spectra. In the present work, however, we focus on K-edge spectra. Even in this simplest case, we find that a previously reported problem with continuum artifacts[58,59] becomes ubiquitous and pervasive in high-quality basis sets. This issue renders the TDKS approach unusable, except in a modified form that is described herein.

2 Theory

This section provides a self-contained description of the TDKS method (Section 2 A), which is not yet widespread for excited-state calculations in molecules. The more common LR-TDDFT approach is introduced briefly in Section 2 B.

2.A. TDKS approach. A rigorous description of TDKS theory from first principles can be found in Refs. 50–52, whereas the present discussion focuses on practical considerations for computing absorption spectra. The adiabatic approximation,[21,51] meaning locality in time, is assumed throughout. As such, the time dependence of the exchange-correlation functional is carried exclusively by the time-evolving density, $\rho(\mathbf{r}, t)$, and ground-state exchange-correlation functionals may be employed without alteration.

2.A.1. Time propagation. The density $\rho(\mathbf{r}, t)$ is represented in terms of time-dependent MOs,

$$\rho(\mathbf{r}, t) = \sum_{k}^{\text{occ}} |\psi_k(\mathbf{r}, t)|^2 \, . \tag{1}$$

Following a perturbation to the ground-state density, introduced at $t = 0$, the MOs $\psi_k(\mathbf{r}, t)$ propagate according to the TDKS equation,

$$\mathrm{i}\hbar \frac{d\psi_k}{dt} = \hat{F}\psi_k(\mathbf{r}, t) \, . \tag{2}$$

This is a one-electron analogue of the time-dependent Schrödinger equation, in which $\hat{F}$ is an effective one-electron Hamiltonian (Fock operator). This equation of motion is integrated numerically in order to obtain the time-evolving MOs $\{\psi_k(\mathbf{r}, t)\}$ from the initial ground-state MOs, the latter of which are eigenfunctions of $\hat{F}$:

$$\hat{F}\psi_k(\mathbf{r}, 0) = \varepsilon_k \psi_k(\mathbf{r}, 0) \, . \tag{3}$$

A perturbative solution of eq. 2 affords the LR-TDDFT equations.[21,24]

Equation (2) for the time-evolving MOs is equivalent to the Liouville-von Neumann equation for the time-dependent one-particle density matrix,

$$\mathrm{i}\hbar \frac{\partial \mathbf{P}}{\partial t} = \mathbf{FP} - \mathbf{PF}^\dagger \, . \tag{4}$$

Here, $\mathbf{P}(t)$ is the matrix representation of $\rho(\mathbf{r}, t)$ in an orthonormal basis, which could be the ground-state MOs determined by eq. 3 or the time-evolved orbitals $\{\psi_k(\mathbf{r}, t)\}$. Formal integration of eq. 4 affords

$$\mathbf{P}(t + \Delta t) = \mathbf{U}(t + \Delta t, t) \, \mathbf{P}(t) \, \mathbf{U}^\dagger(t + \Delta t, t) \tag{5}$$

where $\mathbf{U}(t + \Delta t)$ is a unitary time evolution operator for the time step $t \to t + \Delta t$. Both $\mathbf{P}(t)$ and $\mathbf{F}(t)$ in eq. 4 are time-dependent quantities, which implies that the definition of $\mathbf{U}(t+\Delta t)$ involves time-ordering of $\mathbf{F}(t')$ at points t' along the integration ($t \le t' \le t + \Delta t$), or equivalently a Magnus expansion of nested commutators.[57]

Various forms for $\mathbf{U}(t+\Delta t)$ have been discussed in the literature.[57,60–65] These include adaptive schemes,[65] as well as methods that iterate to self-consistency over the course of a time step from t to $t + \Delta t$.[57] In the present work, we employ the relatively simple modified-midpoint algorithm,[61] which requires only a single (complex-valued) Fock build per time step. This method is stable

when Δt is small, which is required anyway by the energy scales needed to access core-level excitations.

Specifically, Δt determines the highest frequency-domain Fourier component that can described by the finite time series of dipole moment data. The Nyquist sampling theorem[66] limits the signal to frequencies $\omega \leq \omega_{\max}$, where

$$\omega_{\max} = \pi/\Delta t \; . \tag{6}$$

Empirically, we find that well-converged spectra require somewhat smaller time steps,[57] meaning that the spectrum should be considered to be converged only if $E \ll \hbar\omega_{\max}$.

2.A.2. Absorption spectra. The absorption cross section $S(\omega)$ from a TDKS simulation is computed from the imaginary part of the trace of the frequency-dependent polarizability tensor:

$$S(\omega) = \left(\frac{4\pi\omega}{3c}\right) \mathfrak{Im}\big[\alpha_{xx}(\omega) + \alpha_{yy}(\omega) + \alpha_{zz}(\omega)\big] \tag{7}$$

where

$$\alpha_{\lambda\kappa}(\omega) = \frac{\partial \mu_\lambda(\omega)}{\partial \mathcal{E}_\kappa(\omega)} \; . \tag{8}$$

Here, $\lambda, \kappa \in \{x, y, z\}$ and $\alpha_{\lambda_\kappa}(\omega)$ describes the frequency-domain response of the dipole moment (in direction λ) to an applied electric field $\mathcal{E}_\kappa(\omega)$ in direction κ. In practice, the spectrum is obtained (up to an overall constant) as

$$S(\omega) \propto \sum_\lambda |d_\lambda(\omega)|^2 \tag{9}$$

where

$$d_\lambda(\omega) \propto \omega^2 \mu_\lambda(\omega) \tag{10}$$

is the dipole acceleration function.[67] The quantity $\mu_\lambda(\omega)$ is the Fourier transform of $\mu_\lambda(t)$, and in principle it can be used to compute the spectrum directly.[68–70] However, use of the dipole acceleration is thought to be less sensitive to the long-range description of the electron density.[71] This has mostly been examined in strong-field simulations, as in high-harmonic generation.[71–74] Excellent agreement with LR-TDDFT calculations, as documented below, suggests that this approach also works well in the weak-field limit.

The discrete Fourier transform of $\mu_\lambda(t)$ can be expressed as

$$\mu_\lambda(\omega) = \sum_{k=0}^{M} \mu_\lambda(t_k) \; e^{-\mathrm{i}\omega t_k} \; . \tag{11}$$

Here, M is the total number of time steps and $t_k = k\Delta t$. In a TDKS simulation, one computes the time dependent density $\rho(\mathbf{r}, t)$ by solving either eq. 2 or eq. 4, and from $\rho(\mathbf{r}, t)$ one may calculate $\mu_\lambda(t)$ and ultimately the absorption spectrum $S(\omega)$. The frequency resolution of that spectrum improves as the total simulation time ($t_{\max} = M\Delta t$) is increased.

Typical integration time steps on the order of $\Delta t = 0.02$–0.20 a.u..[56–58,75–79] (Note that the atomic unit of time is $\hbar/E_\mathrm{h} \approx 0.0242$ fs.) Values on the smaller end of that range are necessary for XAS, due to the Fourier transform limit on the maximum excitation energy (eq. 6). A total propagation time $t_{\max} = 10$–30 fs is typically required in order to obtain an adequately converged spectrum,[56–58,75–78] which means 30,000–60,000 time steps for XAS simulations.

2.A.3. Padé-accelerated Fourier transforms. Use of a Padé-accelerated transform technique can reduce the simulation time that is required. This method is widely used in magnetic resonance spectroscopy to treat noisy spectra with low resolution,[80,81] and Padé approximants have also been used in other real-time electronic structure calculations.[82–84]

To introduce the Padé technique,[84] we first recognize that eq. 11 for $\mu_\lambda(\omega)$ can be viewed as a polynomial expansion in $z = \exp(-\mathrm{i}\omega\Delta t)$. That is,

$$\mu_\lambda(\omega) = \sum_{k=0}^{M} z^k \mu_\lambda(t_k) = \sum_{k=0}^{M} c_k z^k \tag{12}$$

where $c_k = \mu_\lambda(t_k)$. This power series is then approximated using rational functions of order P,

$$\mu_\lambda(\omega) = \frac{\sum_{k=0}^{P} a_k z^k}{\sum_{l=0}^{P} b_l z^l} \tag{13}$$

where the a_k and b_l are unknown coefficients. Taking the polynomial order to be $P = M/2$, this affords

$$\sum_{k=0}^{P} a_k z^k = \sum_{l=0}^{P} b_l z^l \sum_{m=0}^{M} c_m z^m \; . \tag{14}$$

We take $b_0 = 1$ by convention, thus eq. 14 consists of $2P$ equations for the coefficients $\{a_i, b_i\}$.

The system in eq. 14 is solved by separating the equations according to orders in z. In matrix form, the solution for the coefficients $\{b_i\}$ is

$$\mathbf{b} = \mathbf{G}^{-1}\mathbf{d} \tag{15}$$

where $d_k = -c_{P+k}$ and $\mathbf{G}$ is a $P \times P$ matrix with $G_{kl} = c_{P+k-l}$. The coefficients $\{a_i\}$ are obtained from the $\{b_i\}$ coefficients,

$$a_k = \sum_{l=0}^{k} b_l c_{k-l} \; , \tag{16}$$

then $\mu_\lambda(\omega)$ can be constructed from $\mathbf{a}$ and $\mathbf{b}$. The upshot is that a shorter time sequence of input data is required to obtain a converged Fourier transform.

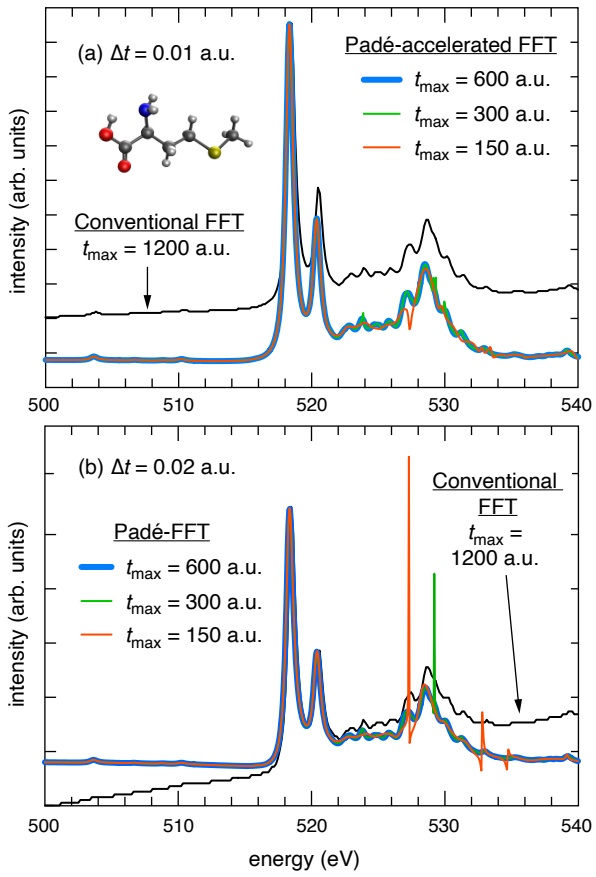

Fig. 1: Absorption spectra of methionine at the oxygen K-edge [B3LYP/6-31+G(d) level], using (a) $\Delta t = 0.01$ a.u. versus (b) $\Delta t = 0.02$ a.u., for various total simulation times $t_{\max}$. Simulation were initiated using a δ-function impulse as described in Section 3 A, and all FFTs use an exponential damping function that broadens the spectra by 0.7 eV. The Padé-accelerated transform is converged at $t_{\max} = 600$ a.u. and is unchanged if the simulation is extended to 1200 a.u..

In contrast to the Padé-accelerated transform technique introduced in Ref. 84, which uses a representation based on occupied–virtual function pairs and applies the Padé technique to components of $\mu_\lambda(t)$ in that representation, the version that we have implemented transforms only the total dipole moment. To demonstrate the technique and to check convergence with respect to total simulation time, we calculated the absorption spectrum of the methionine molecule at the oxygen K-edge (Fig. 1). Results from two different simulations are shown, using either $\Delta t = 0.01$ a.u. or $\Delta t = 0.02$ a.u.. Both values are well within the Nyquist limit for this spectral range, which imposes a bound of $\Delta t \leq 0.16$ a.u. for $E_{\max} = 540$ eV.

Comparing a conventional fast Fourier transform (FFT) to a Padé-accelerated transform, we find that the Padé technique produces a much better converged spectrum in perhaps half the simulation time, meaning $t_{\max} = 600$ a.u. (≈ 14.5 fs). Near-edge features are converged using as little as 150 a.u., although for $t_{\max} \leq 300$ a.u. there are clear artifacts at higher energies. (Such artifacts are not observed using a conventional FFT, but the conventional spectra obtained using $t_{\max} = 600$ a.u. are unable to resolve the pair of peaks centered at 528 eV; see Fig. S1.) Lopata and coworkers suggest that $t_{\max} = 5$ fs (≈ 100 a.u.) is roughly the lower limit of the Padé technique that we have implemented, whereas using separate extrapolations of the occupied–virtual function pairs, they are able to reduce the simulation time to $t_{\max} = 2.5$ fs.[84] Nevertheless, spectra of Ni-porphyrin computed with that technique exhibit artifacts similar to those documented here, around 5 eV above the nitrogen K-edge, even for 5 fs of propagation time.[84]

Artifacts in the Padé-accelerated spectra diminish but do not disappear as the time step is reduced, providing a diagnostic to indicate that additional simulation time is required in order to extend the spectrum into an energy range where artifacts are evident. Additional convergence data are provided in Fig. S2 for an ion-pair dimer that will be considered below. These spectra exhibit small artifacts in the nitrogen K-edge, when $t_{\max} = 200$ a.u., which are not present for $t_{\max} = 600$ a.u.. As with methionine, however, the near-edge features are well-resolved even in the shorter simulation. In view of this, most simulations presented below use at least 600 a.u. of simulation time in order to eliminate any artifacts from Padé extrapolation and thus focus on the appearance of continuum states. In Section 4 C 1, we will revisit whether meaningful near-edge features can be extracted from shorter simulations.

2.A.4. Dipole moment filtering. It will be useful to decompose broadband TDKS spectra according to contributions arising from individual occupied orbitals, or groups thereof, such as the two O(1s) orbitals in the methionine molecule. To do so, we introduce a dipole filtering technique.[58,59]

We first recognize that

$$\mu_\lambda(t) = \mathrm{tr}\big[\mathbf{P}(t)\,\mathbf{D}_\lambda(t)\big] \tag{17}$$

in any orthonormal basis, where $\mathbf{D}_\lambda$ is the matrix representation of the dipole moment operator, $\hat{\mu}_\lambda$. (In practice we will use the time-evolving MO basis.) We can separate $\mu_\lambda(t)$ into a sum of contributions from each occupied MO,

$$\mu_\lambda(t) = \sum_k^{\mathrm{occ}} \mu_{\lambda,k}(t)\ , \tag{18}$$

by filtering out all contributions except for those arising from $\psi_k(\mathbf{r},t)$. In practice this means defining

$$\mu_{\lambda,k}(t) = \mathrm{tr}\big[\mathbf{P}(t)\,\mathbf{D}_{\lambda,k}(t)\big] \tag{19}$$

where the matrix $\mathbf{D}_{\lambda,k}(t)$ consists of the kth row and column of $\mathbf{D}_\lambda(t)$, with zeros elsewhere.

The time-series data $\mu_{\lambda,k}(t)$ admit a Fourier representation analogous to eq. 11, to which one may apply Padé approximants in the same way. The corresponding Fourier transform, $\mu_{\lambda,k}(\omega)$, affords a spectrum that can be associated with occupied MO ψ_k. According to eq. 18 and the linearity of the Fourier transform, the sum of these orbital-indexed spectra must afford the parent TDKS spectrum, but various partitions might be considered. We will always sum together all MOs corresponding to a given elemental edge, meaning that the two O(1s) orbitals or the four C(1s) orbitals in the methionine molecule, for example, will be considered as a group and not decomposed further.

Although the filtering procedure is very simple, there is one important implementation note that warrants mention. Density matrices $\mathbf{P}(t)$ at each time step are not retained because that would represent an intractable amount of storage for realistic molecular calculations. As a result, while there is virtually no overhead for computing arbitrary partitions of the sum in eq. 18, the decision of which partitions to consider must be made at the outset and new partitions cannot be examined in post-processing. That said, it is feasible (if somewhat unwieldy) to store dipole moment data $\mu_{\lambda,k}(t)$ for each individual MO ψ_k. Having done so, arbitrary partitions can be assembled after-the-fact. This functionality exists in our present implementation.

2.B. LR-TDDFT. For completeness, we briefly recapitulate the LR-TDDFT formalism.[21–26] This arises from considering the first-order response of eq. 4 to a perturbation,[21,24] therefore LR-TDDFT may be regarded as the weak-field limit of TDDFT. Identical spectra are obtained with the TDKS approach when the perturbing field is small and the time-dependent simulation is propagated for a sufficiently long time.[56,57]

The LR-TDDFT equation for the excitation energies ω is

$$\begin{pmatrix} \mathbf{A} & \mathbf{B} \\ \mathbf{B}^* & \mathbf{A}^* \end{pmatrix} \begin{pmatrix} \mathbf{x} \\ \mathbf{y} \end{pmatrix} = \omega \begin{pmatrix} \mathbf{1} & \mathbf{0} \\ \mathbf{0} & -\mathbf{1} \end{pmatrix} \begin{pmatrix} \mathbf{x} \\ \mathbf{y} \end{pmatrix} , \tag{20}$$

where the matrices $\mathbf{A}$ and $\mathbf{B}$ are Hessians with respect to orbital rotations.[21] These are given by

$$A_{ia,jb} = (\varepsilon_a - \varepsilon_i)\delta_{ij}\delta_{ab} + \frac{\partial F_{ia}}{\partial P_{jb}} \tag{21a}$$

$$B_{ia,jb} = \frac{\partial F_{ia}}{\partial P_{bj}} . \tag{21b}$$

Indices i and j refer to occupied MOs whereas a and b indicate virtual (unoccupied) MOs. All calculations reported here invoke the Tamm-Dancoff approximation,[21,85] which simplifies eq. 20 by neglecting the de-excitation amplitudes y_{ia}. (These are typically $\sim 100\times$ smaller than the largest excitation amplitudes x_{ia}.) The matrix $\mathbf{B}$ is absent from the resulting eigenvalue problem, which is simply

$$\mathbf{A}\mathbf{x} = \omega\mathbf{x} . \tag{22}$$

This approximation has little effect on XAS spectra (see Fig. S3a) and is used for all LR-TDDFT calculations reported below.

The LR-TDDFT formalism has been adapted for the calculation of core excitation spectra using frozen occupied orbitals,[5,31,86–88] equivalent to a form of CVS approximation. This approximation neglects x_{ia} unless i is a core orbital of interest, *e.g.*, O(1s) or C(1s). Each elemental K-edge is computed separately, using the full virtual space (all ψ_a) but including only the occupied orbitals ψ_i for that particular edge. An example for the oxygen K-edge of methionine (Fig. S3b) demonstrates that the CVS approximation has a negligible effect on excitation energies and oscillator strengths, consistent with other results using many-body theory.[39]

3 Computational Methods

All calculations presented here were obtained using a locally-modified version of Q-Chem,[8] in which we have added dipole filtering to a previous implementation of the TDKS method.[67] We will analyze x-ray spectra in Section 4 but first we present computational details (Section 3 A) and basis-set testing (Section 3 B).

3.A. Functionals and numerical parameters. We set $\Delta t = 0.02$ a.u. for all calculations at the oxygen, nitrogen, and carbon K-edges, which should be adequate even by conservative estimates that are stricter than the Nyquist frequency.[57] Tests using time steps as small as $\Delta t = 0.001$ a.u. demonstrate that oxygen K-edge spectra are converged (Fig. S4). The method of Padé approximants is used to post-process all of the dipole moment data from TDKS simulations. Exponential damping is applied to the time series $\mu_\lambda(t)$, with a damping constant corresponding to spectral broadening of 0.7 eV. As discussed in Section 2 A 3, most of the TDKS spectra reported below are based on $t_{\max} = 600$ a.u. (≈ 14 fs) of propagation time. Whether shorter propagation times can be used in practical calculations is considered in Section 4 C 1.

Starting from a ground-state self-consistent field (SCF) calculation, converged to a threshold of 10^{-8} E_h, the density is perturbed using a δ-function pulse in which the external field is only nonzero during the first two time steps. To normalize the initial perturbation across different choices of Δt, we follow Ref. 67 and report the *integrated* electric field strength $\bar{\boldsymbol{\mathcal{E}}}$, whose components are

$$\bar{\mathcal{E}}_\kappa = \mathcal{E}_\kappa \Delta t \tag{23}$$

for $\kappa \in \{x, y, z\}$. Here, $\mathcal{E}_\kappa$ is the actual field amplitude in the sense of Eq. (8) but that quantity is not needed

to compute the absorption spectrum $S(\omega)$. The perturbing field consists of equal components in each Cartesian direction, which ensures that the perturbation creates a superposition of all excited states regardless of electronic symmetry. We set $\bar{\mathcal{E}}_x = \bar{\mathcal{E}}_y = \bar{\mathcal{E}}_z = 10^{-4}$ a.u. for all TDKS simulations.

Integral screening and shell-pair drop tolerances are set to 10^{-12} a.u. for both TDKS and LR-TDDFT calculations. The latter are converged such that the norm of the residual is $< 10^{-6}$ for each eigenvector $\mathbf{x}$. All calculations are performed on a single 40- or 48-core compute node with 192 Gb of memory.[89]

Many of the spectra presented in Section 4 are computed using a "short-range corrected" (SRC) density functional, SRC1-r1.[90,91] SRC functionals are range-separated hybrids based on the short-range exchange functional μBLYP,[92,93] with range separation parameters adjusted so that LR-TDDFT calculations reproduce experimental K-edge excitation energies.[90,91] These functionals use a large fraction of exact exchange (50% for SRC1-r1) that is attenuated on a length scale < 1 Å.[90] Presumably, this corrects for differential self-interaction error between the core and valence virtual orbitals.

SRC functionals tend to be very accurate for LR-TDDFT calculations (and thus for TDKS calculations), yet this appears to benefit from significant error cancellation, as evidenced by the fact that these functionals perform very poorly in ΔSCF calculations of the same K-edge transitions.[94,95] As such, we have begun to shift our emphasis to functionals such as B3LYP, which performs well in ΔSCF calculations,[94,95] and also to functionals such as PBE0[96] and CAM-B3LYP[97] that perform well for LR-TDDFT[21] and also mitigate problems with long-range charge-transfer states.[21,98–101] LR-TDDFT calculations with B3LYP are often significantly shifted with respect to experiment (by > 10 eV and worse for heavier elements),[90,91,102–105] yet relative peak positions and chemical shifts exhibit accuracy on par with many-body methods.[106] In our view, this observation is consistent with ΔSCF results.[95]

Relativistic corrections are not included in this work. These corrections are $\lesssim 0.5$ eV for second-row elements,[107–109] and while they are larger for later elements our goal here (with regard to heavier elements) is to explore how dipole filtering can disentangle L- and K-edge excitation spectra.

3.B. Basis sets. Several prior studies have explored modified Gaussian basis sets for use in XAS calculations.[110–114] In some cases, standard Gaussian basis sets have been "uncontracted",[110–112] meaning that each Gaussian primitive is used as an independent basis function, improving the variational flexibility for core orbitals. A separate strategy[112–114] is to use basis sets that include core–valence polarization functions, such as the cc-pCVXZ sequence.[115] It has been suggested that these basis sets work well for core-level spectroscopy precisely because the additional polarization functions are uncontracted.[113]

In contrast to the behavior observed using correlated wave functions,[111,114] our test using LR-TDDFT reveal that uncontracting the basis sets modifies the near-edge excitation energies by < 0.1 eV and modifies spectra hardly at all, even at much higher excitation energies (Fig. S5). These tests include the basis sets 6-31+G(d), 6-311(2+,2+)G(d,p), (aug-)cc-pVTZ, aug-cc-pCVTZ, and def2-TZVPD. A previous LR-TDDFT study also concluded that basis-set effects are rather small for XAS calculations but somewhat more pronounced for x-ray emission,[112] because the reference state involves core ionization in that case.[116] (Emission spectra are not considered in the present work.) A summary of basis set effects is presented in Table S1, demonstrating that various SRC functionals predict oxygen and carbon K-edge excitation energies within 0.1–0.2 eV of experiment for small organic molecules. Those deviations are of the same magnitude (or smaller) than relativistic corrections, even for second-row elements.[107–109]

All LR-TDDFT calculations reported below were performed using the CVS approximation. Excitation energies were broadened using a Lorentzian function with a width of 0.7 eV, in order to be directly comparable to spectra obtained from TDKS simulations. The SG-1 numerical quadrature grid[117] is used to integrate the exchange-correlation functional.

4 Results and Discussion

Our major results consist in comparing x-ray spectra obtained using TDKS simulations to those obtained using LR-TDDFT, with the latter calculations performed within the CVS approximation. Some basic comparisons can be found in Section 4 A, following which we describe the use of dipole filtering to identify and remove continuum artifacts in the TDKS spectra (Section 4 B). Some chemically relevant examples are considered in Section 4 C and larger examples (in order to discuss computational cost) are considered in Section 4 D.

4.A. Comparison of TDKS to LR-TDDFT. Good agreement between LR-TDDFT and TDKS has been demonstrated previously for valence excitation spectra,[56,57] however the situation is more complicated for core-level spectra. We begin by comparing the two implementations of TDDFT for simple organic molecules, such as acetone at the carbon or oxygen K-edge (Fig. 2). LR-TDDFT/CVS spectra are computed using either 25 or 100 excited states although the smaller number is sufficient to reproduce the near-edge features. Agreement between LR-TDDFT and TDKS is quantitative so long as enough states are included in the former. Agreement with experiment[118] is also quite good for the near-edge features, because we use the parameterized SRC1-

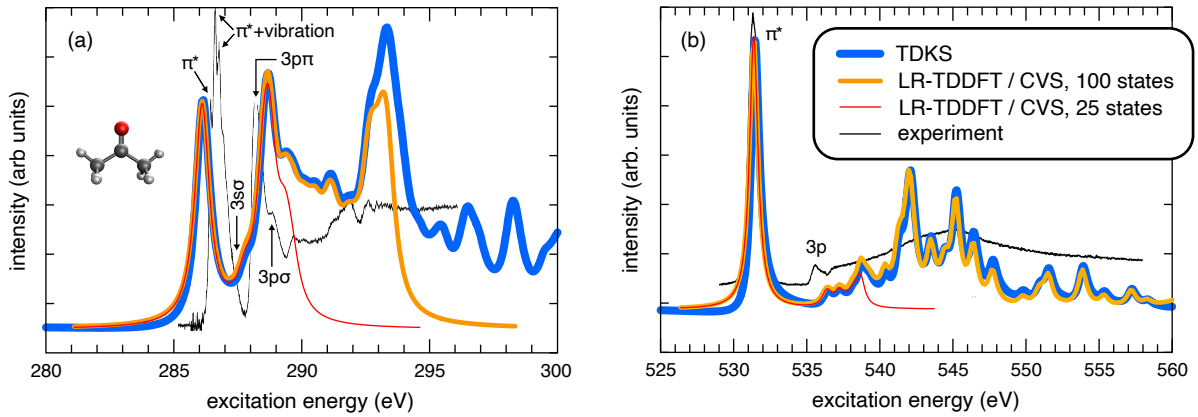

Fig. 2: Absorption spectra of acetone molecule at (a) the carbon K-edge and (b) the oxygen K-edge, computed at the SRC1-r1/6-311(2+,2+)G(d,p) level and compared to experimental spectra that are reproduced from Ref. 118. LR-TDDFT excitation energies are computed using a CVS active space consisting of the three C(1s) MOs, or the O(1s) MO, along with all of the virtual MOs, and each transition is broadened using a Lorentzian function with a 0.7 eV width. TDKS simulations using $\Delta t = 0.02$ a.u. and $t_{\max} = 600$ a.u. were converged using Padé approximants then scaled to match the LR-TDDFT intensity for the first absorption peak. Relativistic effects (not included here) would shift the calculated spectra to higher energy by ≈ 0.1 eV.[107–109] State assignments for the low-lying transitions are taken from Ref. 118.

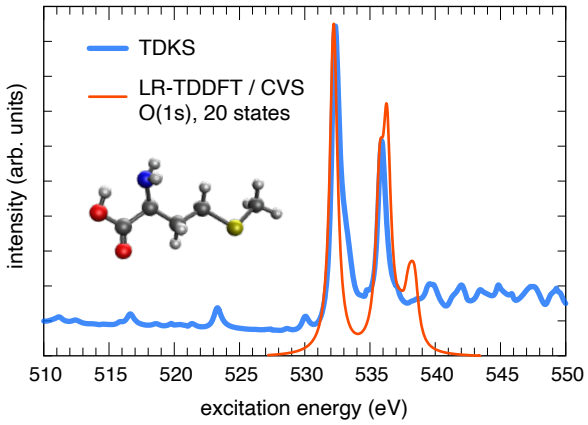

Fig. 3: TDDFT (SRC1-r1/def2-TZVPD) spectra of methionine at the oxygen K-edge. Real-time simulations were propagated for $t_{\max} = 300$ a.u. using $\Delta t = 0.02$ a.u. and converged using Padé approximants. The LR-TDDFT calculation uses a CVS active space consisting of both O(1s) MOs along with all of the virtual MOs, with Lorentzian broadening (0.7 eV). Baselines are offset for clarity. Features below 531 eV in the TDKS spectrum correspond to N(1s) $\rightarrow$ continuum transitions.

r1 functional along with a basis set of reasonable quality. At higher excitation energies, resonances are too shorted-lived to be observed and the experimental spectrum becomes featureless. Structure persists in the TDDFT spectra because all states have infinite lifetimes. Thus, the only meaningful part of the spectra in Fig. 2 is encompassed by about 25 discrete transitions.

For the acetone molecule it is possible to use the TDKS spectrum without filtering but this becomes difficult for larger molecules, especially in high-quality basis sets. This is demonstrated in Fig. 3 for the methionine molecule at the SRC1-r1/def2-TZVPD level. In this case, the TDKS spectrum predicts an intense peak at 532 eV, in quantitative agreement with the O(1s) $\rightarrow$ LUMO transition from a LR-TDDFT/CVS calculation, but several low-intensity "pre-edge" features appear below this feature in the TDKS spectrum. These features are missing from the LR-TDDFT/CVS spectrum, indicating that they do not originate from O(1s) orbitals. Instead, they correspond to excitations from N(1s) orbitals into the highest-energy virtual MOs, which are orthogonalized discretized continuum states rather than valence virtual orbitals.[119] The nature of these excitations becomes clear if one computes all $o \times v$ states afforded by the LR-TDDFT eigenvalue problem (eq. 22), sans CVS approximation, which is feasible for very small molecules in small basis sets. Examining this complete set of transitions, one finds a semi-continuous sequence of states that connects each of the x-ray K-edges (carbon, nitrogen, oxygen, ...) as shown in Fig. S6. These are core $\rightarrow$ continuum excitations. Similar features are called "intruder peaks" in Ref. 84, although we avoid that terminology because it risks confusion with the "intruder states" of multireference perturbation theory,[120,121] which are unrelated.

High-lying excitations to the continuum ought to have exceeding small lifetimes, but in practice they are bound by the finite nature of the basis set. In small basis sets such as 6-31G(d), where one can afford to compute all $o \times v$ states (as in Fig. S6), these transitions to the continuum mostly have very small oscillator strengths, and they are also rather small in the SRC1-r1/def2-TZVPD calculations reported in Fig. 3. However, results presented

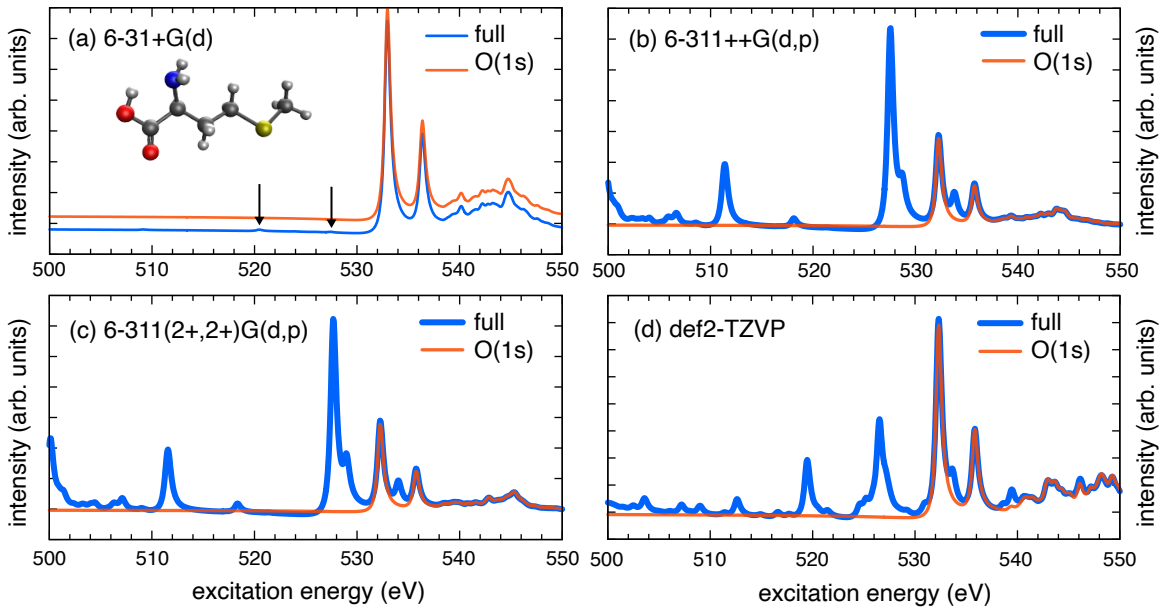

Fig. 4: TDKS spectra for methionine computed using the SRC1-r1 functional in various basis sets: (a) 6-31+G(d), (b) 6-311++G(d,p), (c) 6-311(2+,2+)G(d,p), and (d) def2-TZVP. All simulations used Padé approximants with $t_{\max} = 600$ a.u. and $\Delta t = 0.02$ a.u.. Spectra labeled as "full" are based on the complete dipole moment function whereas those labeled "O(1s)" exclude all contributions except for those originating with the two O(1s) orbitals. Baselines are shifted in (a), with arrows indicating two very weak pre-edge features.

below demonstrate that this is serendipitous, and that these features may acquire significant intensity in higher-quality basis sets. In a complete basis that could describe genuine continuum states, this oscillator strength might disappear because the final state would be infinitely delocalized, but that situation is impossible to achieve using atom-centered basis sets. Alternatively, one might imagine that a complex absorbing potential could be used as a form of open-system boundary condition,[67] in order to suppress the intensity from what are presumably very diffuse excitations. Although this may be explored further in future work, our preliminary experiments with absorbing potentials continued to afford spectra with pre-edge artifacts.[122]

Spurious pre-edge features in Fig. 3 are perhaps easy to identify as such, and therefore to discount, but this may not be true in more complex systems. For example, metal–ligand hybridization in organometallic systems can furnish an intensity borrowing mechanism, leading to the appearance of weakly-allowed 1s → 3d pre-edge transitions.[123] Even for the main K-edge features, the appearance of continuum transitions in the TDKS spectrum degrades the agreement with LR-TDDFT, as evident in the methionine spectrum of Fig. 3 where the agreement between the two forms of TDDFT is less quantitative than it was for acetone.

The appearance of bound → continuum peaks can be avoided in TDKS simulations via *ad hoc* replacement of positive (unbound) SCF eigenvalues with complex-valued eigenvalues, in the MO representation of $\mathbf{P}(t)$.[77,78] This transformation has the effect of giving a finite lifetime to any excitation that involves unbound MOs, and that lifetime can be rendered arbitrarily short by appropriate choice of the imaginary part of the eigenvalue. An alternative might be to introduce a complex absorbing potential.[67,122] Both methods have some arbitrary parameters that must be adjusted, potentially on a case-by-case basis, so we do not pursue these methods here. Instead, we turn to dipole filtering as a diagnostic to understand the origins of the features in a TDKS spectrum.

4.B. Dipole filtering. Figure 4 presents TDKS spectra for methionine, in the region from 500–550 eV, computed using four different basis sets. LR-TDDFT/CVS calculations (not shown) suggest that the O(1s) → LUMO transition should be found at ≈ 532 eV yet several of the TDKS spectra have pronounced features at lower excitation energies.

An oxygen K-edge spectrum can be extracted from these results by filtering on the O(1s) orbitals. In a small basis set such as 6-31+G(d), this has virtually no effect on the spectrum within the indicated energy range (Fig. 4a), and the first peak that is observed is the O(1s) → LUMO transition at 531.9 eV. This suggests that the issue of potential pre-edge artifacts in TDKS spectra may go unnoticed if low-quality basis sets are used. With the benefit of hindsight, one can just barely make out two very weak pre-edge features at 520.6 and 527.4 eV in the SRC1-r1/6-31+G(d) spectrum, but these might eas-

ily have been written off as noise in the absence of further analysis using larger basis sets.

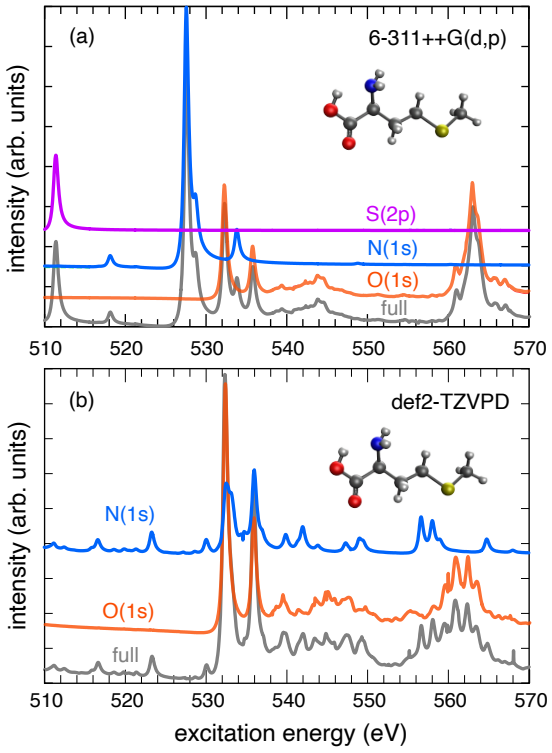

Fig. 5: TDKS spectra for methionine (t_{max} = 300 a.u. and Δt = 0.02 a.u.) computed using SRC-r1 with (a) the 6-311++G(d,p) and (b) the def2-TZVPD basis set. The complete spectrum ("full") is compared to filtered spectra involving only the O(1s), N(1s), or S(2p) orbitals. Baselines have been shifted for clarity but all spectra share a common intensity scale, such that the sum of the filtered spectra equals the full spectrum.

In triple-ζ basis sets the artifacts can no longer be ignored. For example, in the full TDKS spectrum computed at the SRC1-r1/6-311++G(d,p) level (Fig. 4b), it is difficult to determine whether the oxygen K-edge lies at 528 eV or at 532 eV, in the absence of other information. The former peak disappears in the filtered O(1s) spectrum, suggesting that this feature is an artifact of N(1s) $\rightarrow$ continuum transitions. That assignment is confirmed by filtering on the N(1s) orbital, whereas the feature at 511 eV arises from S(2p) orbitals (see Fig. 5a).

Spectra in Fig. 5 are decomposed into elemental contributions, for TDKS calculations using two different basis sets. The complete spectrum is recovered as a sum of O(1s), N(1s), S(2s), and S(2p) contributions, although the S(2s) component is very small and is omitted from Fig. 5a. Relativistic corrections for these elements[107–109] would shift the S(2p) feature in Fig. 5a by +5.4 eV but would not fundamentally alter the picture described here.

Juxtaposition of the spectra in Fig. 5 makes it clear that basis-set effects on the O(1s) $\rightarrow$ LUMO feature at 532 eV are rather small, consistent with the testing reported in Section 3 B. In contrast, N(1s) $\rightarrow$ continuum transitions are extremely sensitive to the choice of basis (see Figs. 4 and 5), which is a general characteristic of discretized continuum states in Gaussian basis sets.[119] In the absence of filtering, there is no way to be confident in the assignment of the K-edge or in the authenticity of any pre-edge features that appear in the spectrum, especially in view of the large absolute peak shifts that often characterize core-level TDDFT calculations.[90,91,102–105]

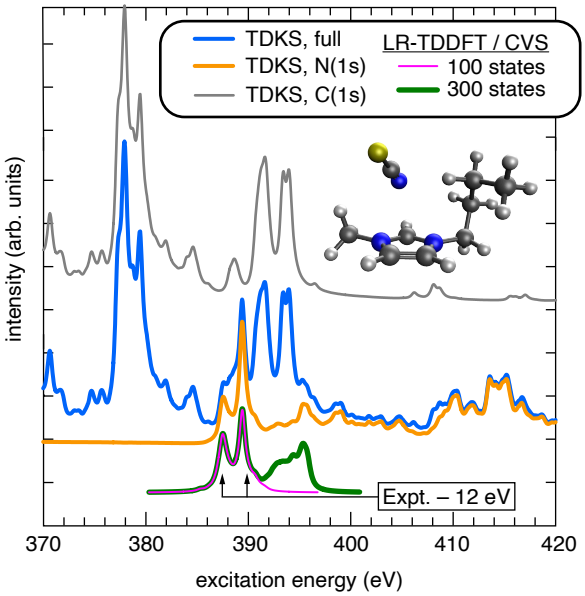

Fig. 6: Absorption spectra near the nitrogen K-edge for the ion-pair dimer [$C_4C_1Im^+$][SCN^-], computed at the B3LYP/6-311(2+,2+)G(d,p) level as described in Fig. 4. Experimental peak maxima (shifted by 12 eV here) are from Ref. 125.

4.C. Chemically relevant examples. Having seen that dipole filtering is essential to remove continuum artifacts in broadband TDKS spectra, we next discuss some chemically-motivated examples where unfiltered spectra (in realistic basis sets) obscure key information.

4.C.1. Ionic liquid ion pair. Our first example is an ion-pair dimer, 1-butyl-3-methylimidazolium ($C_4C_1Im^+$) and thiocyanate (SCN^-), representing a typical dialkylimidazolium ionic liquid.[124] This and other room-temperature ionic liquids have been studied using NEXAFS spectroscopy at the nitrogen and sulfur K-edges.[125] In accompanying calculations, it was observed that excited states could be delocalized across the ion pair in some cases,[125] such that the computational modeling should not be limited to either the cation or the anion.

Spectra shown in Fig. 6 were computed at the B3LYP/6-311(2+,2+)G(d,p) level of theory, for one particular

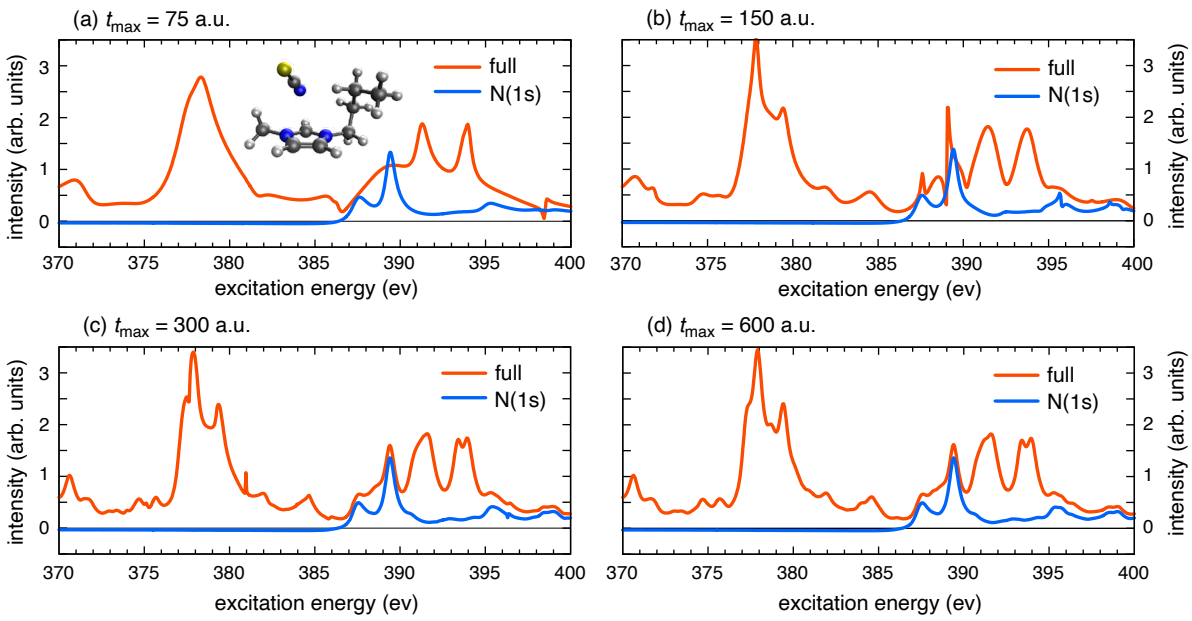

Fig. 7: TDKS spectra near the nitrogen K-edge for $[C_4C_1Im^+][SCN^-]$, computed at the B3LYP/6-311(2+,2+)G(d,p) level using $\Delta t = 0.02$ a.u. with various simulation lengths: (a) $t_{max} = 75$ a.u., (b) $t_{max} = 150$ a.u., (c) $t_{max} = 300$ a.u., and (d) $t_{max} = 600$ a.u.. The spectrum in (d) is the same as that in Fig. 6.

structure of $[C_4C_1Im^+][SCN^-]$. Absent the filtering step, the TDKS spectrum is simply uninterpretable due to significant contamination from C(1s) → continuum excitations. Interloper states contribute spurious, high-intensity pre-edge features as well as other features that overlap with the nitrogen K-edge itself. Upon filtering, a good match is obtained to LR-TDDFT/CVS results, with the nitrogen K-edge appearing at 387.5 eV with a second peak at 389.4 eV. Experimentally, these two features appear at 399.5 eV and 401.9 eV (although they are quite broad),[125] so the spectra in Fig. 6 must be shifted by about 12 eV to match. However, the chemical shift between the two peaks is predicted more accurately: 1.9 eV (theory) versus 2.4 eV (experiment). Note that the $[C_4C_1Im^+][SCN^-]$ dimer exhibits conformation-dependent spectral shifts up to ∼ 1 eV,[125] and we have not attempted any conformational search here.

Dipole filtering recovers good agreement between the two implementations of TDDFT but it is important to consider the cost of either calculation. To do this, we first interrogate the simulation length (t_{max}) that is required to reproduce the experimental features. The TDKS spectrum shown in Fig 6 is a well-converged result based on $t_{max} = 600$ a.u. (≈ 14.5 fs), and in Fig 7 we recompute this spectrum using successively shorter simulations, down to $t_{max} = 75$ a.u. (≈ 1.8 fs). Although some artifacts are certainly evident in the unfiltered TDKS spectra for $t_{max} \leq 300$ a.u., and while these unfiltered spectra differ substantially from one another, the filtered N(1s) spectra are in much better agreement and free of artifacts in the near-edge features. The two peaks that characterize the nitrogen near-edge are well-resolved even in the shortest simulation, and these peaks shift by only ∼ 0.1 eV from $t_{max} = 75$ a.u. to $t_{max} = 600$ a.u.. Monitoring the filtered spectrum thus provides an incisive convergence metric whereas the unfiltered spectrum does not.

When the simulation time is further reduced to $t_{max} = 37.5$ a.u., the peaks that constitute the N(1s) near-edge merge together (Fig. S7), so we take $t_{max} = 75$ a.u. to be the minimum simulation length for this particular application. At the B3LYP/6-311(2+,2+)G(d,p) level, which is 479 basis functions, that amount of simulation requires 6.6 h (wall time) on a single compute node using 20 processor cores, or 4.4 h on 48 cores. By contrast, LR-TDDFT/CVS calculations with $n = 100$ or 300 roots require only 12 and 31 min, respectively, on just 20 cores. Frozen virtual orbital approximations can further accelerate LR-TDDFT calculations (as documented in Section 4 D),[87,88] as can improved iterative eigensolvers,[126–128] whereas no such accelerators are available for TDKS simulations.

That said, the TDKS simulation affords not just the nitrogen K-edge but also the oxygen and carbon edges, whereas each of these requires a separate LR-TDDFT/CVS calculation. The sulfur K-edge, however, would be about 5× more expensive to simulate using the TDKS approach, because at 2,472 eV it requires a 5× decrease in Δt as compared to second-row elements. By contrast, the cost of a LR-TDDFT/CVS calculation involving S(1s) excitation is essentially the same as for N(1s) excitation.

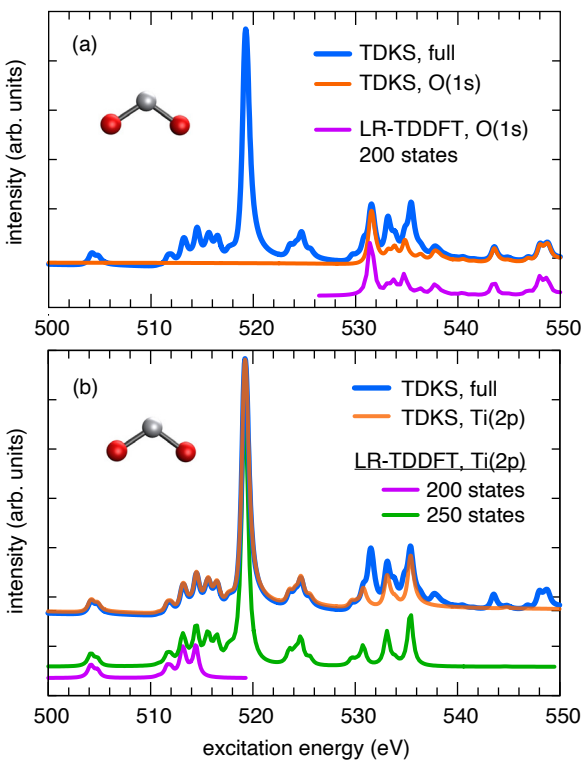

Fig. 8: Absorption spectra for the TiO_2 molecule computed using TDDFT at the SRC1-r1/def2-TZVPD level. Real-time simulations used $\Delta t = 0.02$ a.u. and $t_{max} = 1200$ a.u., with results filtered according to (a) the O(1s) orbitals, to obtain the oxygen K-edge, or else (b) Ti(2p) orbitals, revealing the titanium L-edge. LR-TDDFT spectra use a CVS active space consisting of either O(1s) or Ti(2p) orbitals plus the full virtual space. Baselines are offset for clarity.

4.C.2. TiO_2. We next consider the isolated TiO_2 molecule as a very simple example of a transition metal oxide. This is an interesting case because the metal L-edge overlaps with the oxygen K-edge in these non-relativistic calculations. In general, L-edge spectra require the treatment of spin-orbit coupling, to describe the splitting of the 2p states into $2p_{3/2}$ and $2p_{1/2}$,[3,38,129] but this is not considered in the present work where our goal is simply to compare TDKS and LR-TDDFT results.

Figure 8 plots TiO_2 excitation spectra in the range 500–550 eV, computed at the SRC1-r1/def2-TZVPD level. Given the large shifts that are often required to match experiment, it is not obvious which feature in the full TDKS spectrum constitutes the O(1s) $\rightarrow$ LUMO transition. For example, results above indicate that the SRC1-r1 functional places the oxygen K-edge around 532 eV, but for TiO_2 described at the B3LYP/def2-TZVPD level the O(1s) $\rightarrow$ LUMO excitation appears at 515 eV and there is a band of transitions from 515–520 eV. There are prominent features in the same energy region in the SRC-r1 spectra shown in Fig. 8, but dipole filtering reveals that these are not associated with O(1s) excitations but arise instead from Ti(2p) orbitals, which constitute the most intense bands in the spectrum. The oxygen K-edge appears around 532 eV but includes significant contamination from the titanium L-edge. This is easily filtered away to expose separate oxygen and titanium spectra, either of which is a good match to the corresponding LR-TDDFT/CVS calculation.

Even when dipole filtering is applied, the TDKS simulation is based on a time-evolving density matrix that includes all of the occupied MOs at every time step. As such, quantitative agreement with LR-TDDFT/CVS calculations demonstrates that there is essentially no error in the CVS approximation in the examples that we consider. This observation is significant, because whereas the CVS approximation has been carefully benchmarked for K-edge spectra,[39,40] less is known about its accuracy for L- and M-edge spectra. In those cases, initial-state orbitals may not be energetically well separated from other occupied MOs, leading to larger errors when the CVS approximation is invoked. In principle, interior eigenvalue solvers[40–42] could be used to address the veracity of the CVS approximation, but this has so far been done only in a very limited way.[40] Although we do not see any evidence for a breakdown of the CVS approximation for the L-edge of TiO_2, the question needs to be examined in other systems. TDKS simulations provide a means to obtain spectra that do not invoke any active-space approximation. Those benchmarks may be expensive, however, as we document in the next section using test systems that resemble more realistic applications of TDDFT.

4.D. Larger systems and cost comparison. Lastly, we consider some larger examples that constitute realistic use cases for a molecular (non-periodic) TDDFT code. These include hydrated uracil clusters (Section 4 D 1), as examples of insulators where the system is larger than those considered above but where the excited states remain relatively localized. We also consider nanoclusters of titania (Section 4 D 2) where the electronic structure is more delocalized.

4.D.1. Hydrated uracil clusters. Even for small organic chromophores, LR-TDDFT spectra of an aqueous-phase solute may converge slowly with respect to the number of water molecules included in the calculation.[130] This has been documented for valence excitations but the sensitivity likely originates in the virtual orbitals, so similar sensitivity is expected in XAS calculations. Here, we consider (uracil)$(H_2O)_N$ clusters with $N = 21$ or 68 water molecules, taken from a molecular dynamics simulation.[98] Spectra are computed at the nitrogen K-edge, meaning that the active occupied orbitals within the CVS approximation are localized on the solute and these tests probe how the spectra and the computational effort change as the environment is enlarged. Figure 9 reports spectra from both LR-TDDFT/CVS and TDKS

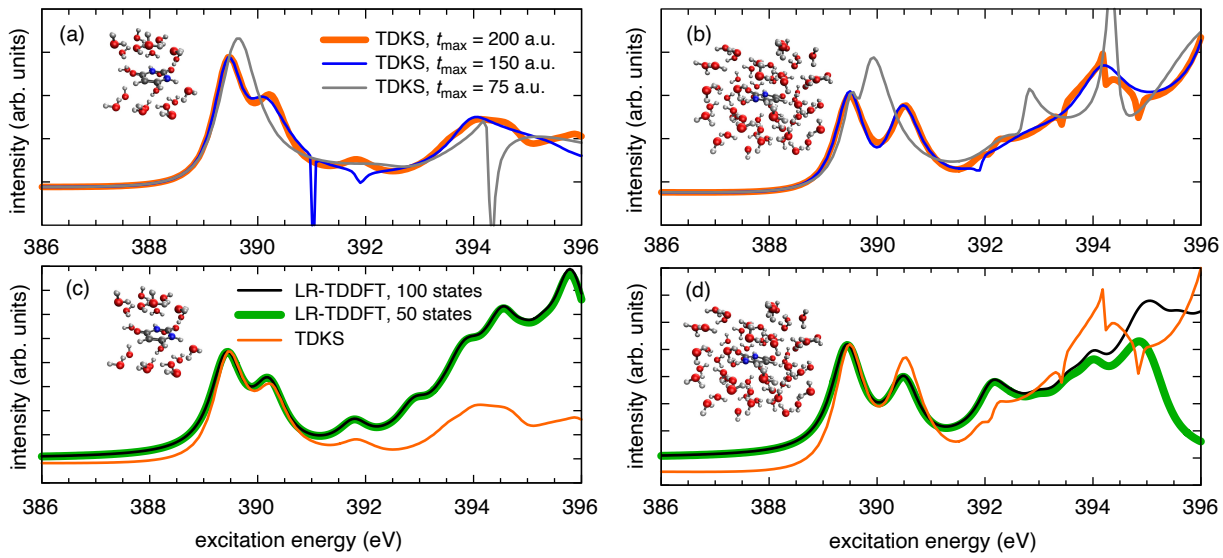

Fig. 9: TDDFT spectra at the nitrogen K-edge for hydrated uracil clusters: (a) TDKS for (uracil)$(H_2O)_{21}$ and (b) TDKS for (uracil)$(H_2O)_{68}$, comparing different simulations times, t_{max}; (c) LR-TDDFT compared to TDKS for the smaller cluster, and (d) LR-TDDFT compared to TDKS for the larger cluster. All calculations were performed the CAM-B3LYP/6-31G(d) level usingg $\Delta t = 0.02$ a.u. for TDKS and a CVS active space for LR-TDDFT. Legends on the left also apply to panels on the right.

calculations for these two clusters.

In contrast to the $[C_4C_1Im^+][SCN^-]$ system considered above, for the present example we find that 75 a.u. of time propagation is insufficient to resolve the narrower splitting of the near-edge peaks (see Figs. 9a and 9b), for which 150 a.u. is required. These features are obtained much more easily using LR-TDDFT/CVS calculations, requiring only $n = 50$ states even for the larger cluster. The agreement between the two methods is satisfactory for the near-edge features provided that $t_{max} \gtrsim 150$ a.u.. The calculations with $N = 21$ and $N = 68$ water molecules involve 508 and 1401 basis functions, respectively, and require 5.9 h and 37.5 h for the full 200 a.u. of simulation time, running on 40 processors of a single compute node. In contrast, LR-TDDFT/CVS calculations running on just 20 processors require 5 min for the smaller cluster and 53 min for the larger one, if $n = 100$ states are requested, or about half that time to compute the $n = 50$ states that comprise the near-edge features.

To understand these timing data, consider the computational bottlenecks in either calculation. In LR-TDDFT, the cost arises from matrix–vector products of $\mathbf{A}$ with asymmetric pseudo-density matrices representing the vectors $\mathbf{x}$ in eq. 22.[44,45] These contractions are performed in an integral-direct fashion[25,43–45] and the cost of any one of them is essentially the same as one (complex-valued) Fock build in ground-state DFT.[25] We use a Davidson eigensolver, employing a standard algorithm where one new subspace vector is added for each non-converged eigenvector at each iteration.[28,30] As such, the maximum number of matrix–vector products is $n \times n_{iter}(n_{iter} + 1)/2$ for a calculation that requires n_{iter} iterations to converge. (We do not perform any kind of subspace collapse, as this can hamper convergence.[30]) As an example, the (uracil)$(H_2O)_{68}$ calculation requesting $n = 100$ eigenvalues requires $n_{iter} = 6$ iterations and a total of 1,950 matrix–vector products. Naively, one might assume that the cost of these contractions would be 1,950 Fock-build equivalents, but in reality it is significantly less than that due to the use of a block-Davison algorithm.[28,30] In this approach, all subspace vectors are digested with each batch of electron repulsion integrals,[25,45] meaning that integrals are not recomputed for each subspace vector. This analysis is predicated on the assumption that all of the subspace vectors can be stored in memory, and all LR-TDDFT timing data reflect that situation. We will return to this point in the next section.

The cost of a TDKS simulation reflects one complex-valued Fock build per time step, when using the modified-midpoint algorithm for the time propagation.[61] For $\Delta t = 0.02$ a.u. and $t_{max} = 150$ a.u., which was the minimum required to resolve the near-edge features in these uracil–water cluters, this means 7,500 Fock-build equivalents. That is more than an order of magnitude more builds than the comparable LR-TDDFT calculation, and moreover does not benefit from the batching that is possible within a block-Davidson eigensolver. Use of incremental Fock builds might accelerate the TDKS simulations,[131] but we have not implemented such an algorithm.

Virtual orbital cutoffs have been suggested as a means to reduce the cost of large LR-TDDFT calculations.[87,88] Since the bottleneck steps are performed in the atomic orbital basis, however, this does not reduce the integrals cost unless it can introduce sparsity into the pseudo-

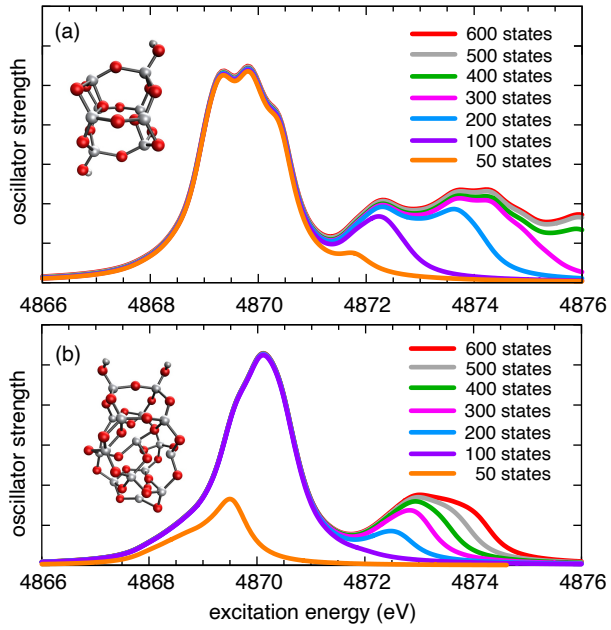

Fig. 10: LR-TDDFT/CVS spectra at the titanium K-edge for (a) $Ti_8O_{16}H_2$ and (b) $Ti_{16}O_{32}H_2$, computed at the PBE0/def2-SV(P) level.

densities, but the systems considered here are probably too small to reap much benefit from this. A cutoff may accelerate convergence, however, by reducing the amount of mixing in the virtual space, and we do find that to be the case for these systems. Retaining only those virtual orbitals with $\varepsilon_a < 0.5\ E_\mathrm{h}$ eliminates 86% of the virtual MOs, which is more aggressive than cutoffs pursued in other work,[87,88] yet we find that peak positions are essentially unchanged (Fig. S8). The cutoff accelerates the convergence, requiring only 596 matrix–vector contractions for (uracil)$(H_2O)_{68}$ as compared to 1,950 when the complete virtual space is employed. LR-TDDFT/CVS timings are thereby reduced to 1 min for the smaller cluster and 26 min for the larger one, computing $n = 100$ states on 20 processors.

4.D.2. Titania clusters. As a final example, we consider $Ti_8O_{16}H_2$ and $Ti_{16}O_{32}H_2$ clusters that were taken from Ref. 132 then passivated with hydrogen atoms. LR-TDDFT/CVS spectra at the titanium K-edge are plotted in Fig. 10, computing up to $n = 600$ excited states. For the larger cluster, a minimum of 400 states is required to converge the position of the second absorption maximum at 4,873 eV, whereas only 100 states are needed to converge the leading feature.

For $Ti_{16}O_{32}H_2$ (836 basis functions), the calculation with $n = 500$ states required 13,649 matrix–vector products and was completed in 6.3 h on 20 processors. A virtual orbital cutoff of 0.5 E_h introduces negligible change in the spectrum (Fig. S9) but does not accelerate convergence. Nevertheless, in view of the considerations discussed above we may safely conclude that LR-TDDFT will be significantly faster than any TDKS calculation with $\gtrsim 10,000$ time steps. Assuming a five-fold reduction in Δt to reach the titanium K-edge, this would mean that a cost-competitive TDKS simulation could reach only $t_\mathrm{max} \lesssim 40$ a.u. (≈ 1 fs). This is too little simulation time to reliably obtain a spectrum, even with Padé approximants. In short, we conclude that LR-TDDFT is likely *always* significantly faster than the corresponding TDKS calculations, provided that the subspace vectors required for the former can be stored in shared memory. Disk-based or distributed-memory algorithms complicate this comparison, so if the number of states is large enough that the subspace cannot be held in memory, then TDKS offers an alternative algorithm with a very low memory footprint but a very high floating-point operation cost.

5 Conclusions

This work examines the use of TDKS or "real-time" TDDFT simulations for core-level spectroscopy. The TDKS approach seems attractive for this application because multiple elemental x-ray edges can be computed at once, in a single broadband calculation, up to an energy scale that varies inversely with the time step that is used to integrate the equations of motion. In practice, however, TDKS spectra are contaminated with transitions to the continuum, to the point that they are often uninterpretable. A filtering step restores interpretability by decomposing the full spectrum into components defined by subsets of the MOs, and meaningful NEXAFS spectra can be recovered.

However, even when Padé approximants are used to process the TDKS data, reducing the requisite simulation time to $\sim$ 2–4 fs, the cost of the time propagation remains more than an order of magnitude larger that the cost of conventional LR-TDDFT. This is supported by both theoretical analysis and empirical timing data, when the LR-TDDFT calculation is performed using a CVS-style active-space approximation that excludes most of the occupied MOs. Therefore, we suggest that the utility of the TDKS approach for core-level spectroscopy may lie in the fact that it obviates the need to invoke a CVS approximation, which is (by contrast) ubiquitous in LR-TDDFT and other eigenvalue-based approaches to core-level spectroscopy.[34–37] At least within the realm of DFT, TDKS simulations may therefore provide benchmarks to assess the accuracy of active-space approximations, which remain relatively untested for XAS at elemental L- and M-edges. This will require careful processing of the TDKS data in order to avoid contamination by continuum artifacts.

Supporting Information

Basis-set testing and additional convergence results, along with coordinates for the test systems considered.

Acknowledgments

This work was supported by National Science Foundation grant nos. CHE-1665322 and CHE-1955282. Calculations were performed at the Ohio Supercomputer Center.[89]

Author Declarations

J.M.H. serves on the board of directors of Q-Chem Inc.

Author Contributions

John M. Herbert: Conceptualization (lead); Data curation (equal); Formal analysis (lead); Funding acquisition (lead); Investigation (equal); Methodology (equal); Project administration (lead); Software (contributing); Supervision (lead); Validation (equal); Visualization (lead); Writing – original draft (lead); Writing – review and editing (lead). **Ying Zhu:** Investigation (equal); Methodology (equal); Software (lead). **Bushra Alam:** Data curation (equal); Formal analysis (contributing); Investigation (equal); Methodology (contributing); Validation (equal); Visualization (contributing); Writing – original draft (contributing). **Avik Kumar Ojha:** Investigation (contributing); Data curation (contributing).

References

[1] Norman, P.; Dreuw, A. Simulating x-ray spectroscopies and calculating core-excited states of molecules. *Chem. Rev.* **2018,** *118,* 7208–7248.

[2] Bokarev, S. I.; Kühn, O. Theoretical x-ray spectroscopy of transition metal compounds. *WIREs Comput. Mol. Sci.* **2020,** *10,* e1433.

[3] Kasper, J. M.; Stetina, T. F.; Jenkins, A. J.; Li, X. *Ab initio* methods for L-edge x-ray absorption spectroscopy. *Chem. Phys. Rev.* **2020,** *1,* 011304.

[4] Besley, N. A. Density functional theory based methods for the calculation of x-ray spectroscopy. *Acc. Chem. Res.* **2020,** *53,* 1306–1315.

[5] Besley, N. A. Modeling of the spectroscopy of core electrons with density functional theory. *WIREs Comput. Mol. Sci.* **2021,** *12,* e1527.

[6] Rankine, C. D.; Penfold, T. J. Progress in the theory of x-ray spectroscopy: From quantum chemistry to machine learning and ultrafast dynamics. *J. Phys. Chem. A* **2021,** *125,* 4276–4293.

[7] Klein, B. P.; Hall, S. J.; Mauer, R. J. The nuts and bolts of core-hole constrained *ab initio* simulation for K-shell x-ray photoemission and absorption spectra. *J. Phys.: Condens. Matt.* **2021,** *33,* 154005.

[8] Epifanovsky, E.; Gilbert, A. T. B.; Feng, X.; Lee, J.; Mao, Y.; Mardirossian, N.; Pokhilko, P.; White, A. F.; Coons, M. P.; Dempwolff, A. L.; Gan, Z.; Hait, D.; Horn, P. R.; Jacobson, L. D.; Kaliman, I.; Kussmann, J.; Lange, A. W.; Lao, K. U.; Levine, D. S.; Liu, J.; McKenzie, S. C.; Morrison, A. F.; Nanda, K. D.; Plasser, F.; Rehn, D. R.; Vidal, M. L.; You, Z.-Q.; Zhu, Y.; Alam, B.; Albrecht, B. J.; Aldossary, A.; Alguire, E.; Andersen, J. H.; Athavale, V.; Barton, D.; Begam, K.; Behn, A.; Bellonzi, N.; Bernard, Y. A.; Berquist, E. J.; Burton, H. G. A.; Carreras, A.; Carter-Fenk, K.; Chakrabory, R.; Chien, A. D.; Closser, K. D.; Cofer-Shabica, V.; Dasgupta, S.; de Wergifosse, M.; Deng, J.; Diedenhofen, M.; Do, H.; Ehlert, S.; Fang, P.-T.; Fatehi, S.; Feng, Q.; Friedhoff, T.; Gayvert, J.; Ge, Q.; Gidofalvi, G.; Goldey, M.; Gomes, J.; González-Espinoza, C. E.; Gulania, S.; Gunina, A. O.; Hanson-Heine, M. W. D.; Harbach, P. H. P.; Hauser, A.; Herbst, M. F.; Hernández Vera, M.; Hodecker, M.; Holden, Z. C.; Houck, S.; Huang, X.; Hui, K.; Huynh, B. C.; Ivanov, M.; Jász, Á.; Ji, H.; Jiang, H.; Kaduk, B.; Kähler, S.; Khistyaev, K.; Kim, J.; Kis, G.; Klunzinger, P.; Koczor-Benda, Z.; Koh, J. H.; Kosenkov, D.; Koulias, L.; Kowalczyk, T.; Krauter, C. M.; Kue, K.; Kunitsa, A.; Kus, T.; Ladjánszki, I.; Landau, A.; Lawler, K. V.; Lefrancois, D.; Lehtola, S.; Li, R. R.; Li, Y.-P.; Liang, J.; Liebenthal, M.; Lin, H.-H.; Lin, Y.-S.; Liu, F.; Liu, K.-Y.; Loipersberger, M.; Luenser, A.; Manjanath, A.; Manohar, P.; Mansoor, E.; Manzer, S. F.; Mao, S.-P.; Marenich, A. V.; Markovich, T.; Mason, S.; Maurer, S. A.; McLaughlin, P. F.; Menger, M. F. S. J.; Mewes, J.-M.; Mewes, S. S.; Morgante, P.; Mullinax, J. W.; Oosterbaan, K. J.; Paran, G.; Paul, A. C.; Paul, S. K.; Pavošević, F.; Pei, Z.; Prager, S.; Proynov, E. I.; Rák, Á.; Ramos-Cordoba, E.; Rana, B.; Rask, A. E.; Rettig, A.; Richard, R. M.; Rob, F.; Rossomme, E.; Scheele, T.; Scheurer, M.; Schneider, M.; Sergueev, N.; Sharada, S. M.; Skomorowski, W.; Small, D. W.; Stein, C. J.; Su, Y.-C.; Sundstrom, E. J.; Tao, Z.; Thirman, J.; Tornai, G. J.; Tsuchimochi, T.; Tubman, N. M.; Veccham, S. P.; Vydrov, O.; Wenzel, J.; Witte, J.; Yamada, A.; Yao, K.; Yeganeh, S.; Yost, S. R.; Zech, A.; Zhang, I. Y.; Zhang, X.; Zhang, Y.; Zuev, D.; Aspuru-Guzik, A.; Bell, A. T.; Besley, N. A.; Bravaya, K. B.; Brooks, B. R.; Casanova, D.; Chai, J.-D.; Coriani, S.; Cramer, C. J.; Cserey, G.; DePrince III, A. E.; DiStasio Jr., R. A.; Dreuw, A.; Dunietz, B. D.; Furlani, T. R.; Goddard III, A.; Hammes-Schiffer, S.; Head-Gordon, T.; Hehre, W. J.; Hsu, C.-P.; Jagau, T.-C.; Jung, Y.; Klamt, A.; Kong, J.; Lambrecht, D. S.; Liang, W.; Mayhall, N. J.; McCurdy, C. W.; Neaton, J. B.; Ochsenfeld, C.; Parkhill, J. A.; Peverati, R.; Rassolov, V. A.; Shao, Y.; Slipchenko, L. V.; Stauch, T.; Steele, R. P.; Subotnik, J. E.; Thom, A. J. W.; Tkatchenko, A.; Truhlar, D. G.; Van Voorhis, T.; Wesolowski, T. A.; Whaley, K. B.; Woodcock III, H. L.; Zimmerman, P. M.; Faraji, S.; Gill, P. M. W.; Head-Gordon, M.; Herbert, J. M.; Krylov, A. I. Software for the frontiers of quantum chemistry: An overview of developments in the Q-Chem 5 package. *J. Chem. Phys.* **2021,** *155,* 084801.

[9] Nascimento, D. R.; Govind, N. Computational approaches for XANES, VtC-XES, and RIXS using linear-response time-dependent density functional theory based methods. *Phys. Chem. Chem. Phys.* **2022,** *24,* 14680–14691.

[10] Popmintchev, T.; Chen, M.-C.; Popmintchev, D.; Arpin, P.; Brown, S.; Ališauskas, S.; Andriukaitis, G.; Balčiunas, T.; Mücke, O. D.; Pugzlys, A.; Baltuška, A; Shim, B.; Schrauth, S. E.; Gaeta, A.; Hernández-García, C.; Plaja, L.; Becker, A.; Jaroon-Becker, A.; Murnane, M. M.; Kapteyn, H. C. Bright coherent ultrahigh harmonics in the keV x-ray regime from mid-infrared femtosecond lasers. *Science* **2012,** *336,* 1287–1291.

[11] Miaja-Avila, L.; O'Neil, G. C.; Uhlig, J.; Cromer, C. L.; Dowell, M. L.; Jimenez, R.; Hoover, A. S.; Silverman, K. L.; Ullom, J. N. Laser plasma x-ray source for ultrafast time-resolved x-ray absorption spectroscopy. *Struct. Dynam.* **2015,** *2,* 024301.

[12] Schoenlein, R.; Elsaesser, T.; Holldack, K.; Huang, Z.; Kapteyn, H.; Murnane, M.; Woerner, M. Recent advances in ultrafast x-ray sources. *Phil. Trans. R. Soc. A* **2019,** *377,* 20180384.

[13] Geneaux, R.; Marroux, H. J. B.; Guggenmos, A.; Neumark, D. M.; Leone, S. R. Transient absorption spectroscopy using high harmonic generation: A review of ultrafast x-ray dynamics in molecules and solids. *Phil. Trans. R. Soc. A* **2019,** *377,* 20170463.

[14] Depresseux, A.; Oliva, E.; Gautier, J.; Tissandier, F.; Nejdl, J.; Kozlova, M.; Maynard, G.; Goddet, J. P.; Tafzi, A.; Lifschitz, A.; Kim, H. T.; Jacquemot, S.; Malka, V.; Phuoc, K. T.; Thaury, C.; Rousseau, P.; Iaquaniello, G.; Lefrou, T.; Flacco, A.; Vodungbo, B.; Lambert, G.; Rousse, A.; Zeitoun, P.; Sebban, S. Table-top femtosecond x-ray laser by collisional ionization gating. *Nat. Photonics* **2015,** *9,* 817–822.

[15] Smith, J. W.; Saykally, R. J. Soft x-ray absorption spectroscopy of liquids and solutions. *Chem. Rev.* **2017,** *117,* 13909–13934.

[16] Kleine, C.; Ekimova, M.; Goldsztejn, G.; Raabe, S.; Strüber, C.; Ludwig, J.; Yarlagadda, S.; Eisebitt, S.; Vrakking, M. J. J.; Elsaesser, T.; Nibbering, E. T. J.; Rouzée, A. Soft x-ray absorption spectroscopy of aqueous solutions using a table-top femtosecond soft x-ray source. *J. Phys. Chem. Lett.* **2019,** *10,* 52–58.

[17] Suzuki, T. Ultrafast photoelectron spectroscopy of aqueous solutions. *J. Chem. Phys.* **2019,** *151,* 090901.

[18] Smith, A. D.; Balčiūnas, T.; Chang, Y.-P.; Schmidt, C.; Zinchenko, K.; Nunes, F. B.; Rossi, E.; Svoboda, V.; Yin, Z.; Wolf, J.-P.; Wörner, H. J. Femtosecond soft-x-ray absorption spectroscopy of liquids with a water-window high-harmonic source. *J. Phys. Chem. Lett.* **2020,** *11,* 1981–1988.

[19] Cirri, A.; Husek, J.; Biswas, S.; Baker, L. R. Achieving surface sensitivity in ultrafast XUV spectroscopy: $M_{2,3}$-edge reflection–absorption of transition metal oxides. *J. Phys. Chem. C* **2017,** *121,* 15861–15869.

[20] Palacios, A.; Martín, F. The quantum chemistry of attosecond molecular science. *WIREs Comput. Mol. Sci.* **2020,** *10,* e1430.

[21] Herbert, J. M. Density-functional theory for electronic excited states. In *Theoretical and Computational Photochemistry: Fundamentals, Methods, Applications and Synergy with Experimental Approaches*; García-Iriepa, C.; Marazzi, M., Eds.; Elsevier: 2023; Chapter 3, pages 69–118.

[22] Casida, M. E. Time-dependent density functional response theory for molecules. In *Recent Advances in Density Functional Methods, Part I*, Vol. I; Chong, D. P., Ed.; World Scientific: River Edge, NJ, 1995; Chapter 5, pages 155–192.

[23] Casida, M. E. Time-dependent density functional response theory of molecular systems: Theory, computational methods, and functionals. In *Recent Developments and Applications of Modern Density Functional Theory*, Vol. 4; Seminario, J. M., Ed.; Elsevier: Amsterdam, 1996.

[24] Furche, F. On the density matrix based approach to time-dependent density functional response theory. *J. Chem. Phys.* **2001,** *114,* 5982–5992.

[25] Furche, F.; Rappoport, D. Density functional methods for excited states: Equilibrium structure and electronic spectra. In *Computational Photochemistry*, Vol. 16; Olivucci, M., Ed.; Elsevier: Amsterdam, 2005; Chapter 3, pages 93–128.

[26] Elliott, P.; Furche, F.; Burke, K. Excited states from time-dependent density functional theory. In *Reviews in Computational Chemistry*, Vol. 26; Lipkowitz, K. B.; Cundari, T. R., Eds.; Wiley-VCH: New York, 2009; Chapter 3, pages 91–165.

[27] Olsen, J.; Jensen, H. J. A.; Jørgensen, P. Solution of the large matrix equations which occur in response theory. *J. Comput. Phys.* **1988,** *74,* 265–282.

[28] Crouzeix, M.; Philippe, B.; Sadkane, M. The Davidson method. *SIAM J. Sci. Comput.* **1994,** *15,* 62–76.

[29] Stratmann, R. E.; Scuseria, G. E.; Frisch, M. J. An efficient implementation of time-dependent density-functional theory for the calculation of excitation energies of large molecules. *J. Chem. Phys.* **1998,** *109,* 8218–8224.

[30] Leininger, M. L.; Sherrill, C. D.; Allen, W. D.; Schaefer III, H. F. Systematic study of selected diagonalization methods for configuration interaction matrices. *J. Comput. Chem.* **2001,** *22,* 1574–1589.

[31] Stener, M.; Fronzoni, G.; de Simone, M. Time dependent density functional theory of core electrons excitations. *Chem. Phys. Lett.* **2003,** *373,* 115–123.

[32] Cederbaum, L. S.; Domcke, W.; Schirmer, J. Many-body theory of core holes. *Phys. Rev. A* **1980,** *22,* 206–222.

[33] Barth, A.; Cederbaum, L. S. Many-body theory of core-valence excitations. *Phys. Rev. A* **1981,** *23,* 1038–1061.

[34] Coriani, S.; Koch, H. Communication: X-ray absorption spectra and core-ionization potentials within a core-valence separated coupled cluster framework. *J. Chem. Phys.* **2015,** *143,* 181103.

[35] Wenzel, J.; Holzer, A.; Wormit, M.; Dreuw, A. Analysis and comparison of CVS-ADC approaches up to third order for the calculation of core-excited states. *J. Chem. Phys.* **2015,** *142,* 214104.

[36] Vidal, M. L.; Feng, X.; Epifanovsky, E.; Krylov, A. I.; Coriani, S. New and efficient equation-of-motion coupled-cluster framework for core-excited and core-ionized states. *J. Chem. Theory Comput.* **2019,** *15,* 3117–3133.

[37] Mazin, I. M.; Sokolov, A. Y. Core-excited states and x-ray absorption spectra from multireference algebraic diagrammatic construction theory. *J. Chem. Theory Comput.* **2023** (in press; DOI: 10.1021/acs.jctc.3c00477).

[38] Bussy, A.; Hutter, J. Efficient and low-scaling linear-response time-dependent density functional theory implementation for core-level spectroscopy of large and periodic systems. *Phys. Chem. Chem. Phys.* **2021,** *23,* 4736–4746.

[39] Herbst, M. F.; Fransson, T. Quantifying the error of the core–valence separation approximation. *J. Chem. Phys.* **2020,** *153,* 054114.

[40] Helmich-Paris, B. Simulating X-ray absorption spectra with complete active space self-consistent field linear response methods. *Int. J. Quantum Chem.* **2021,** *121,* e26559.

[41] Zuev, D.; Vecharynski, E.; Yang, C.; Orms, N.; Krylov, A. I. New algorithms for iterative matrix-free eigensolvers in quantum chemistry. *J. Comput. Chem.* **2015,** *36,* 273–284.

[42] Kasper, J. M.; Williams-Young, D. B.; Vecharynski, E.; Yang, C.; Li, X. A well-tempered hybrid method for solving challenging time-dependent density functional theory (TDDFT) systems. *J. Chem. Theory Comput.* **2018,** *14,* 2034–2041.

[43] Weiss, H.; Ahlrichs, R.; Häser, M. A direct algorithm for self-consistent-field linear response theory and application to C_{60}: Excitation energies, oscillator strengths, and frequency-dependent polarizabilities. *J. Chem. Phys.* **1993,** *99,* 1262–1270.

[44] Maurice, D. R. *Single Electron Theories of Excited States,* Thesis, University of California, 1998.

[45] Morrison, A. F.; Epifanovsky, E.; Herbert, J. M. Double-buffered, heterogeneous CPU + GPU integral digestion algorithm for single-excitation calculations involving a large number of excited states. *J. Comput. Chem.* **2018,** *39,* 2173–2182.

[46] Morrison, A. F.; You, Z.-Q.; Herbert, J. M. Ab initio implementation of the Frenkel-Davydov exciton model: A naturally parallelizable approach to computing collective excitations in crystals and aggregates. *J. Chem. Theory Comput.* **2014,** *10,* 5366–5376.

[47] Morrison, A. F.; Herbert, J. M. Low-scaling quantum chemistry approach to excited-state properties via an *ab initio* exciton model: Application to excitation energy transfer in a self-assembled nanotube. *J. Phys. Chem. Lett.* **2015,** *6,* 4390–4396.

[48] Gao, M.; Paul, S.; Schwieters, C. D.; You, Z.-Q.; Shao, H.; Herbert, J. M.; Parquette, J. R.; Jaroniec, C. P. A structural model for a self-assembled nanotube provides insight into its exciton dynamics. *J. Phys. Chem. C* **2015,** *119,* 13948–13956.

[49] Gross, E. K. U.; Kohn, W. Time-dependent density functional theory. *Adv. Quantum Chem.* **1990,** *21,* 255–291.

[50] Gross, E. K. U.; Ullrich, C. A.; Gossmann, U. J. Density functional theory of time-dependent systems. In *Density Functional Theory*; Gross, E. K. U.; Dreizler, R. M., Eds.; Plenum Press: New York, 1995; pages 149–171.

[51] Gross, E. K. U.; Maitra, N. T. Introduction to TDDFT. In *Fundamentals of Time-Dependent Density Functional Theory*, Vol. 837; Marques, M. A. L.; Maitra, N. T.; Nogueira, F. M. S.; Gross, E. K. U.; Rubio, A., Eds.; Springer-Verlag: Heidelberg, 2012; Chapter 4, pages 53–97.

[52] Ullrich, C. A.; Yang, Z. H. A brief compendium of time-dependent density functional theory. *Braz. J. Phys.* **2014,** *44,* 154–188.

[53] Baer, R.; Kronik, L. Time-dependent generalized Kohn–Sham theory. *Eur. Phys. J. B* **2018,** *91,* 170.

[54] Provorse, M. R.; Isborn, C. M. Electron dynamics with real-time time-dependent density functional theory. *Int. J. Quantum Chem.* **2016,** *116,* 739–749.

[55] Li, X.; Govind, N.; Isborn, C.; DePrince III, A. E.; Lopata, K. Real-time time-dependent electronic structure theory. *Chem. Rev.* **2020,** *120,* 9951–9993.

[56] Tussupbayev, S.; Govind, N.; Lopata, K.; Cramer, C. J. Comparison of real-time and linear-response time-dependent density functional theories for molecular chromophores ranging from sparse to high densities of states. *J. Chem. Theory Comput.* **2015,** *11,* 1102–1109.

[57] Zhu, Y.; Herbert, J. M. Self-consistent predictor/corrector algorithms for stable and efficient integration of the time-dependent Kohn-Sham equation. *J. Chem. Phys.* **2018,** *148,* 044117.

[58] Kadek, M.; Konecny, L.; Gao, B.; Repisky, M.; Ruud, K. X-ray absorption resonances near $L_{2,3}$-edges from real-time propagation of the Dirac–Kohn–Sham density matrix. *Phys. Chem. Chem. Phys.* **2015,** *17,* 22566–22570.

[59] Yang, M.; Sissay, A.; Chen, M.; Lopata, K. Intruder peak-free transient inner-shell spectra using real-time simulations. *J. Chem. Theory Comput.* **2022,** *18,* 992–1002.

[60] Castro, A.; Marques, M. A. L.; Rubio, A. Propagators for the time-dependent Kohn–Sham equations. *J. Chem. Phys.* **2004,** *121,* 3425–3433.

[61] Li, X.; Smith, S. M.; Markevitch, A. N.; Romanov, D. A.; Levis, R. J.; Schlegel, H. B. A time-dependent Hartree–Fock approach for studying the electronic optical response of molecules in intense fields. *Phys. Chem. Chem. Phys.* **2005,** *7,* 233–239.

[62] Williams-Young, D.; Goings, J. J.; Li, X. Accelerating real-time time-dependent density functional theory with a nonrecursive Chebyshev expansion of the quantum propagator. *J. Chem. Theory Comput.* **2016,** *12,* 5333–5338.

[63] Blanes, S.; Casas, F.; Murua, A. Symplectic time-average propagators for the Schrödinger equation with a time-dependent Hamiltonian. *J. Chem. Phys.* **2017,** *146,* 114109.

[64] Pueyo, A. G.; Marques, M. A. L.; Rubio, A.; Castro, A. Propagators for the time-dependent Kohn–Sham equations: Multistep, Runge–Kutta, exponential Runge–Kutta, and commutator free Magnus method. *J. Chem. Theory Comput.* **2018,** *14,* 3040–3052.

[65] Ye, L.; Wang, H.; Zhang, Y.; Liu, W. Self-adaptive real-time time-dependent density functional theory for core excitations. *J. Chem. Phys.* **2022,** *157,* 074106.

[66] Oppenheim, A. V. *Discrete-Time Signal Processing;* Pearson Education: Upper Saddle River, New Jersey, 3rd ed.; 1999.

[67] Zhu, Y.; Herbert, J. M. High harmonic spectra computed using time-dependent Kohn-Sham theory with Gaussian orbitals and a complex absorbing potential. *J. Chem. Phys.* **2022,** *156,* 204123.

[68] Diestler, D. J. Harmonic generation: Quantum-electrodynamical theory of the harmonic photon-number spectrum. *Phys. Rev. A* **2008,** *78,* 033814.

[69] Baggesen, J. C.; Madsen, L. B. On the dipole, velocity and acceleration forms in high-order harmonic generation from a single atom or molecule. *J. Phys. B: At. Mol. Opt. Phys.* **2011,** *44,* 115601.

[70] Coccia, E.; Mussard, B.; Labeye, M.; Caillat, J.; Taïeb, R.; Toulouse, J.; Luppi, E. Gaussian continuum basis functions for calculating high-harmonic generation spectra. *Int. J. Quantum Chem.* **2016,** *116,* 1120–1131.

[71] Chu, X.; Memoli, P. J. Role of multiphoton excitation and two-electron effects in high harmonic generation of H_2: A TDDFT calculation. *Chem. Phys.* **2011,** *391,* 83–87.

[72] Burnett, K.; Reed, V. C.; Cooper, J.; Knight, P. L. Cal-

culation of the background emitted during high-harmonic generation. *Phys. Rev. A* **1992,** *45,* 3347–3349.
[73] Kamta, G. L.; Bandrauk, A. D. Three-dimensional time-profile analysis of high-order harmonic generation in molecules: Nuclear interferences in H_2^+. *Phys. Rev. A* **2005,** *71,* 053407.
[74] Chirilă, C. C.; Lein, M. Assessing different forms of the strong-field approximation for harmonic generation in molecules. *J. Mod. Opt.* **2007,** *54,* 1039–1045.
[75] Lopata, K.; Govind, N. Modeling fast electron dynamics with real-time time-dependent density functional theory: Application to small molecules and chromophores. *J. Chem. Theory Comput.* **2011,** *7,* 1344–1355.
[76] Lopata, K.; Van Kuiken, B. E.; Khalil, M.; Govind, N. Linear-response and real-time time-dependent density functional theory studies of core-level near-edge x-ray absorption. *J. Chem. Theory Comput.* **2012,** *8,* 3284–3292.
[77] Lopata, K.; Govind, N. Near and above ionization electronic excitations with non-Hermitian real-time time-dependent density functional theory. *J. Chem. Theory Comput.* **2013,** *9,* 4939–4946.
[78] Fernando, R. G.; Balhoff, M. C.; Lopata, K. X-ray absorption in insulators with non-Hermitian real-time time-dependent density functional theory. *J. Chem. Theory Comput.* **2015,** *11,* 646–654.
[79] Goings, J. J.; Li, X. An atomic orbital based real-time time-dependent density functional theory for computing electronic circular dichroism band spectra. *J. Chem. Phys.* **2016,** *144,* 234102.
[80] Hansen, E. S. S.; Kim, S.; Miller, J. J.; Geferath, M.; Morrell, G.; Laustsen, C. Fase Padé transform accelerated CSI for hyperpolarized MRS. *Tomography* **2016,** *2,* 117–124.
[81] Belkić, D.; Belkić, K. Review of recent applications of the conventional and derivative fast Padé transform for magnetic resonance spectroscopy. *J. Math. Chem.* **2019,** *57,* 385–464.
[82] Goings, J. J.; Kasper, J. M.; Egidi, F.; Sun, S.; Li, X. Real time propagation of the exact two component time-dependent density functional theory. *J. Chem. Phys.* **2016,** *145,* 104107.
[83] Nascimento, D. R.; DePrince, III, A. E. Simulation of near-edge X-ray absorption fine structure with time-dependent equation-of-motion coupled-cluster theory. *J. Phys. Chem. Lett.* **2017,** *8,* 2951–2957.
[84] Bruner, A.; LaMaster, D.; Lopata, K. Accelerated broadband spectra using transition dipole decomposition and Padé approximants. *J. Chem. Theory Comput.* **2016,** *12,* 3741–3750.
[85] Hirata, S.; Head-Gordon, M. Time-dependent density functional theory within the Tamm-Dancoff approximation. *Chem. Phys. Lett.* **1999,** *314,* 291–299.
[86] Lestrange, P. J.; Nguyen, P. D.; Li, X. Calibration of energy-specific TDDFT for modeling K-edge XAS spectra of light elements. *J. Chem. Theory Comput.* **2015,** *11,* 2994–2999.
[87] Besley, N. A. Fast time-dependent density functional theory calculations of the x-ray absorption spectroscopy of large systems. *J. Chem. Theory Comput.* **2016,** *12,* 5018–5025.
[88] Hanson-Heine, M. W. D.; George, M. W.; Besley, N. A. Assessment of time-dependent density functional theory calculations with the restricted space approximation for excited state calculations of large systems. *Mol. Phys.* **2018,** *116,* 1452–1459.
[89] Ohio Supercomputer Center, http://osc.edu/ark:/19495/f5s1ph73 (accessed 2023-08-05).
[90] Besley, N. A.; Peach, M. J. G.; Tozer, D. J. Time-dependent density functional theory calculations of near-edge x-ray absorption fine structure with short-range corrected functionals. *Phys. Chem. Chem. Phys.* **2009,** *11,* 10350–10358.
[91] Besley, N. A.; Asmuruf, F. A. Time-dependent density functional theory calculations of the spectroscopy of core electrons. *Phys. Chem. Chem. Phys.* **2010,** *12,* 12024–12039.
[92] Rohrdanz, M. A.; Herbert, J. M. Simultaneous benchmarking of ground- and excited-state properties with long-range-corrected density functional theory. *J. Chem. Phys.* **2008,** *129,* 034107.
[93] Richard, R. M.; Herbert, J. M. Time-dependent density-functional description of the ^1L_a state in polycyclic aromatic hydrocarbons: Charge-transfer character in disguise? *J. Chem. Theory Comput.* **2011,** *7,* 1296–1306.
[94] Jana, S.; Herbert, J. M. Slater transition methods for core-level electron binding energies. *J. Chem. Phys.* **2023,** *158,* 094111.
[95] Jana, S.; Herbert, J. M. Fractional-electron and transition-potential methods for core-to-valence excitation energies using density functional theory. *J. Chem. Theory Comput.* **2023,** *19,* 4100–4113.
[96] Adamo, C.; Barone, V. Toward reliable density functional methods without adjustable parameters: The PBE0 model. *J. Chem. Phys.* **1999,** *110,* 6158–6170.
[97] Yanai, T.; Tew, D. P.; Handy, N. C. A new hybrid exchange-correlation functional using the Coulomb-attenuating method (CAM-B3LYP). *Chem. Phys. Lett.* **2004,** *393,* 51–57.
[98] Lange, A.; Herbert, J. M. Simple methods to reduce charge-transfer contamination in time-dependent density-functional calculations of clusters and liquids. *J. Chem. Theory Comput.* **2007,** *3,* 1680–1690.
[99] Lange, A. W.; Rohrdanz, M. A.; Herbert, J. M. Charge-transfer excited states in a π-stacked adenine dimer, as predicted using long-range-corrected time-dependent density functional theory. *J. Phys. Chem. B* **2008,** *112,* 6304–6308.
[100] Lange, A. W.; Herbert, J. M. Both intra- and interstrand charge-transfer excited states in B-DNA are present at energies comparable to, or just above, the $^1\pi\pi^*$ excitonic bright states. *J. Am. Chem. Soc.* **2009,** *131,* 3913–3922.
[101] Isborn, C. M.; Mar, B. D.; Curchod, B. F. E.; Tavernelli, I.; Martínez, T. J. The charge transfer problem in density functional theory calculations of aqueously solvated molecules. *J. Phys. Chem. B* **2013,** *117,* 12189–12201.
[102] Nakata, A.; Imamura, Y.; Otsuka, T.; Nakai, H. Time-dependent density functional theory calculations for core-excited states: Assessment of standard exchange-correlation functionals and development of a novel hybrid functional. *J. Chem. Phys.* **2006,** *124,* 094105.
[103] Nakata, A.; Imamura, Y.; Nakai, H. Hybrid exchange-correlation functional for core, valence, and Rydberg excitations: Core-valence-Rydberg B3LYP. *J. Chem. Phys.* **2006,** *125,* 064109.
[104] Nakata, A.; Imamura, Y.; Nakai, H. Extension of the core-valence-Rydberg B3LYP functional to core-excited-

state calculations of third-row atoms. *J. Chem. Theory Comput.* **2007,** *3,* 1295–1305.
[105] Roemelt, M.; Beckwith, M. A.; Duboc, C.; Collomb, M.-N.; Neese, F.; DeBeer, S. Manganese K-edge x-ray absorption spectroscopy as a probe of metal–ligand interactions in coordination compounds. *Inorg. Chem.* **2012,** *51,* 680–687.
[106] Fransson, T.; Brumboiu, I. E.; Vidal, M. L.; Norman, P.; Coriani, S.; Dreuw, A. XABOOM: An x-ray absorption benchmark of organic molecules based on carbon, nitrogen, and oxygen 1s $\rightarrow \pi^*$ transitions. *J. Chem. Theory Comput.* **2021,** *17,* 1618–1637.
[107] Asmuruf, F. A.; Besley, N. A. Calculation of near-edge x-ray absorption fine structure with the CIS(D) method. *Chem. Phys. Lett.* **2008,** *463,* 267–271.
[108] Takahashi, O. Relativistic corrections for single- and double-core excitations at the K- and L-edges from Li to Kr. *Comput. Theor. Chem.* **2017,** *1102,* 80–86.
[109] Yao, Y.; Golze, D.; Rinke, P.; Blum, V.; Kanai, Y. All-electron BSE@*GW* method for *K*-edge core electron excitation energies. *J. Chem. Theory Comput.* **2022,** *18,* 1569–1583.
[110] Besley, N. A.; Gilbert, A. T. B.; Gill, P. M. W. Self-consistent-field calculations of core excited states. *J. Chem. Phys.* **2009,** *130,* 124308.
[111] Sarangi, R.; Vidal, M. L.; Coriani, S.; Krylov, A. I. On the basis set selection for calculations of core-level states: Different strategies to balance cost and accuracy. *Mol. Phys.* **2020,** *118,* e1769872.
[112] Fouda, A. E. A.; Besley, N. A. Assessment of basis sets for density functional theory-based calculations of core-electron spectroscopies. *Theor. Chem. Acc.* **2018,** *137,* 6.
[113] Ambroise, M. A.; Jensen, F. Probing basis set requirements for calculating core ionization and core excitation spectroscopy by the Δ self-consistent-field approach. *J. Chem. Theory Comput.* **2019,** *15,* 325–337.
[114] Ambroise, M. A.; Dreuw, A.; Jensen, F. Probing basis set requirements for calculating core ionization and core excitation spectra using correlated wave function methods. *J. Chem. Theory Comput.* **2021,** *17,* 2832–2842.
[115] Woon, D. E.; Dunning Jr., T. H. Gaussian basis sets for use in correlated molecular calculations. V. Core-valence basis sets for boron through neon. *J. Chem. Phys.* **1995,** *103,* 4572–4585.
[116] Hanson-Heine, M. W. D.; George, M. W.; Besley, N. A. Basis sets for the calculation of core-electron binding energies. *Chem. Phys. Lett.* **2018,** *699,* 279–285.
[117] Gill, P. M. W.; Johnson, B. G.; Pople, J. A. A standard grid for density-functional calculations. *Chem. Phys. Lett.* **1993,** *209,* 506–512.
[118] Prince, K. C.; Richter, R.; de Simone, M.; Alagia, M.; Coreno, M. Near edge x-ray absorption spectra of some small polyatomic molecules. *J. Phys. Chem. A* **2003,** *107,* 1955–1963.
[119] Herbert, J. M. The quantum chemistry of loosely-bound electrons. In *Reviews in Computational Chemistry*, Vol. 28; Parill, A. L.; Lipkowitz, K., Eds.; Wiley-VCH: Hoboken, 2015; Chapter 8, pages 391–517.
[120] Choe, Y.-K.; Witek, H. A.; Finley, J. P.; Hirao, K. Identifying and removing intruder states in multireference Møller–Plesset perturbation theory. *J. Chem. Phys.* **2001,** *114,* 3913–3918.
[121] Witek, H. A.; Choe, Y.-K.; Finley, J. P.; Hirao, K. Intruder state avoidance multireference Møller–Plesset perturbation theory. *J. Comput. Chem.* **2002,** *23,* 957–965.
[122] Zhu, Y.; Alam, B.; Herbert, J. M. Broadband x-ray absorption spectra from time-dependent Kohn-Sham calculations. *ChemRxiv* **2021,** DOI: 10.26434/chemrxiv.14766960.v1.
[123] de Groot, F.; Kotani, A. *Core Level Spectroscopy of Solids;* CRC Press: Boca Raton, 2008.
[124] Gousseva, E.; Midgley, S. D.; Seymour, J. M.; Seidel, R.; Grau-Crespo, R.; Lovelock, K. R. J. Understanding x-ray photoelectron spectra of ionic liquids: Experiments and simulations of 1-butyl-3-methylimidazolium thiocyanate. *J. Phys. Chem. B* **2022,** *126,* 10500–10509.
[125] Fogerty, R. M.; Matthews, R. P.; andd C. R. Ashworth, M. T. C.; Brandt-Talbot, A.; Corbett, P. J.; Palgrave, R. G.; andd T. W. Chamberlain, R. A. B.; Hoogerstaete, T. V.; Johnson, P. B. J.; Hunt, P. A.; Besley, N. A.; Lovelock, K. R. J. NEXAFS spectroscopy of ionic liquids: Experiments versus calculations. *Phys. Chem. Chem. Phys.* **2017,** *19,* 31156–31167.
[126] Furche, F.; Krull, B. T.; Nguyen, B. D.; Kwon, J. Accelerating molecular property calculations with nonorthonormal Krylov space methods. *J. Chem. Phys.* **2016,** *144,* 174105.
[127] Vecharynski, E.; Brabec, J.; Shao, M.; Govind, N.; Yang, C. Efficient block preconditioned eigensolvers for linear response time-dependent density functional theory. *Comput. Phys. Commun.* **2017,** *221,* 42–52.
[128] Zhou, Z.; Parker, S. M. Accelerating molecular property calculations with semiempirical preconditioning. *J. Chem. Phys.* **2021,** *155,* 204111.
[129] Konecny, L.; Vicha, J.; Komorovsky, S.; Ruud, K.; Repisky, M. Accurate x-ray absorption spectra near L- and M-edges from relativistic four-component damped response time-dependent density functional theory. *Inorg. Chem.* **2022,** *61,* 830–846.
[130] Milanese, J. M.; Provorse, M. R.; Alameda, Jr., E.; Isborn, C. M. Convergence of computed aqueous absorption spectra with explicit quantum mechanical solvent. *J. Chem. Theory Comput.* **2017,** *13,* 2159–2171.
[131] Liang, W.; Chapman, C. T.; Li, X. Efficient first-principles electronic dynamics. *J. Chem. Phys.* **2011,** *134,* 184102.
[132] Cho, D.; Ko, K. C.; Lamiel-García, O.; Bromley, S. T.; Lee, J. Y.; Illas, F. Effect of size and structure on the ground-state and excited-state electronic structure of TiO_2 nanoparticles. *J. Chem. Theory Comput.* **2016,** *12,* 3751–3763.

Table of Contents Graphic